JCB Journal of Cell Biology

ARTICLE

Myosin VI and branched actin filaments mediate membrane constriction and fission of melanosomal tubule carriers

Léa Ripoll[1], Xavier Heiligenstein[1], Ilse Hurbain[1,2], Lia Domingues[1], Florent Figon[1,3], Karl J. Petersen[4], Megan K. Dennis[5,6], Anne Houdusse[4], Michael S. Marks[5,6], Graça Raposo[1,2], and Cédric Delevoye[1,2]

Vesicular and tubular transport intermediates regulate organellar cargo dynamics. Transport carrier release involves local and profound membrane remodeling before fission. Pinching the neck of a budding tubule or vesicle requires mechanical forces, likely exerted by the action of molecular motors on the cytoskeleton. Here, we show that myosin VI, together with branched actin filaments, constricts the membrane of tubular carriers that are then released from melanosomes, the pigment containing lysosome-related organelles of melanocytes. By combining superresolution fluorescence microscopy, correlative light and electron microscopy, and biochemical analyses, we find that myosin VI motor activity mediates severing by constricting the neck of the tubule at specific melanosomal subdomains. Pinching of the tubules involves the cooperation of the myosin adaptor optineurin and the activity of actin nucleation machineries, including the WASH and Arp2/3 complexes. The fission and release of these tubules allows for the export of components from melanosomes, such as the SNARE VAMP7, and promotes melanosome maturation and transfer to keratinocytes. Our data reveal a new myosin VI– and actin-dependent membrane fission mechanism required for organelle function.

Introduction

Intracellular trafficking among endomembrane organelles and the plasma membrane occurs primarily via tubular or vesicular carriers. Formation of these carriers requires membrane deformation at multiple steps, including the generation of membrane curvature to form a bud, extension of the bud to form the tubule or vesicle, and scission to release the carrier (Anitei and Hoflack, 2011). These steps require motor-dependent forces along microtubules and actin filaments (F-actin; Anitei and Hoflack, 2011).

Theoretical models for vesicle scission predict that actin polymerization and/or myosin motor activity generates forces that facilitate membrane fission (Liu et al., 2006; Simunovic et al., 2017). In cells, F-actin dynamics coincide with and promote the release of tubular intermediates from the plasma membrane (Römer et al., 2010), whereas myosin II (perhaps with myosin Vb) contributes to the fission of TGN-derived tubules (Miserey-Lenkei et al., 2010; Liu et al., 2013). Myosin VI (Myo6) has also been proposed to participate in fission events at the TGN (Warner et al., 2003) or the plasma membrane (Buss et al., 2001), but a direct role for Myo6 has not yet been demonstrated. Whether actin and associated myosins remodel the membrane to support the physical separation of the transport intermediate from the source membrane is not understood. Additionally, whether such severing activity might affect organelle function remains to be determined.

Myo6 is unique among mammalian myosin motors in that it moves toward the minus end of F-actin (Wells et al., 1999). Importantly, Myo6 does not only move membrane carriers, but also tethers them to the actin cytoskeleton (Altman et al., 2004). Myo6 supports critical functions at multiple cellular sites via different adaptors that target it to plasma membrane–derived vesicles (Dab2 and GIPC; Dance et al., 2004; Naccache et al., 2006; Spudich et al., 2007) or to endosomes, autophagosomes, or Golgi (e.g., LMTK2, TOM1, and optineurin; Sahlender et al., 2005; Au et al., 2007; Chibalina et al., 2007; Tumbarello et al.,

[1]Structure and Membrane Compartments, Institut Curie, Paris Sciences & Lettres Research University, Centre National de la Recherche Scientifique, UMR144, Paris, France; [2]Cell and Tissue Imaging Facility, Institut Curie, Paris Sciences & Lettres Research University, Centre National de la Recherche Scientifique, UMR144, Paris, France; [3]Master BioSciences, École Normale Supérieure de Lyon, Université Claude Bernard Lyon 1, Université de Lyon, Lyon, France; [4]Structural Motility, Institut Curie, Paris Sciences & Lettres Research University, Centre National de la Recherche Scientifique, UMR144, Paris, France; [5]Department of Pathology and Laboratory Medicine, Children's Hospital of Philadelphia, Philadelphia, PA; [6]Departments of Pathology and Laboratory Medicine and Physiology, University of Pennsylvania, Philadelphia, PA.

Correspondence to Cédric Delevoye: cedric.delevoye@curie.fr; M.K. Dennis' present address is Dept. of Biology, Marist College, Poughkeepsie, NY; F. Figon's present address is Institut de Recherche sur la Biologie de l'Insecte, Centre National de la Recherche Scientifique, UMR7261, University of Tours, Tours, France.

2012). Among them, optineurin is a multidomain protein that can modulate signaling pathways as well as various trafficking events (Slowicka et al., 2016). For example, Myo6 cooperates with optineurin and controls Golgi morphology and post-Golgi trafficking (Sahlender et al., 2005), plasma membrane fusion of secretory vesicles (Bond et al., 2011), autophagosome–lysosome fusion (Tumbarello et al., 2012), or endosomal cargo sorting (Au et al., 2007). Nevertheless, the molecular mechanisms underlying the various cellular activities of Myo6 are still poorly characterized, and whether optineurin is needed to recruit Myo6 onto membranes or to modulate its activity is not understood.

Lysosome-related organelles (LROs) are cell type–specific membrane-bound compartments that share features with endosomes and lysosomes and fulfill physiologically important functions (Marks et al., 2013). Melanosomes, the LROs of skin epidermal melanocytes and eye pigment cells, function in the synthesis and storage of melanin pigments. Within melanocytes, melanosomes originate from endosomes and progressively mature into fully pigmented organelles (Raposo et al., 2001) that are ultimately secreted and transferred to neighboring epidermal keratinocytes (Delevoye, 2014; Wu and Hammer, 2014). Melanosomes are unique in that the melanin biopolymer deposited on a rigid proteinaceous matrix, and filling their lumen, may impose a particular stiffness to their limiting membrane. On the other hand, melanosomes are dynamic sorting stations that resemble endosomes; they constantly receive membranous components from endocytic and secretory pathways (Marks et al., 2013; Patwardhan et al., 2017) and recycle materials such as SNARE proteins through tubular carriers (Dennis et al., 2016). Although actin polymerization and myosins are thought to contribute to the remodeling of stiff membranes (Jonsdottir and Li, 2004; Sirotkin et al., 2005; Aghamohammadzadeh and Ayscough, 2009; Boulant et al., 2011), how the melanosome reshapes its membrane to recycle components is unknown. Moreover, the morphological features of these melanosomal recycling tubules, the mechanisms underlying their formation and fission, and their function during pigmentation are not well understood.

We previously showed that Myo6 associates with pigmented melanosomes where it regulates local actin dynamics (Loubéry et al., 2012). Myo6 does not move melanosomes along F-actin but rather controls melanosome maturation through an unknown process (Loubéry et al., 2012). Here, we show that Myo6 controls the fission of membrane tubules from melanosomes that were previously shown to function in SNARE recycling (Dennis et al., 2016). Severing of the tubules requires the constriction of the neck at specific melanosomal subdomains, which is mediated by Myo6 motor activity. Pinching of the tubules involves the cooperation of optineurin and the activity of actin nucleation machineries such as the WASH (Wiskott-Aldrich syndrome protein and SCAR homolog) and Arp2/3 complexes. This process not only facilitates cargo export for melanosome maturation but also ensures its homeostasis and function, including the secretion and transfer of melanin pigment to recipient keratinocytes. This study thus uncovers an unprecedented role for Myo6 and actin dynamics in the constriction of membranes required for the fission of tubular transport intermediates and organelle function.

Results

Myo6 promotes the release of melanosomal tubules

We first investigated the role of Myo6 in melanosome membrane remodeling by addressing the dynamics of the SNARE VAMP7, the only membrane component known to recycle from melanosomes via tubular intermediates (Dennis et al., 2016). As described in mouse melanocytes (Jani et al., 2015; Dennis et al., 2016), exogenously expressed mCherry-VAMP7 (mCh-VAMP7) in MNT-1 human melanoma cells localized primarily to melanosomes (Fig. 1 A, arrows) and colocalized with the melanogenic enzyme Tyrosinase-related protein-1 fused to GFP (GFP-TYRP1, Fig. S1, A and B, arrowheads; Pearson's correlation coefficient, P = 0.88). Also, mCh-VAMP7 was frequently detected in a single tubular structure (Fig. 1 B and Video 1, arrowheads) emerging from the melanosome core (Fig. 1 B and Video 1, arrows). These tubules were recently defined as intermediates in cargo recycling from melanosomes (Dennis et al., 2016) and, as shown in Fig. 1 B, they separated from melanosomes (red arrow) within a few seconds of their formation (Fig. 1 C; 4.7 ± 0.9 s). Strikingly, siRNA-mediated depletion of Myo6 (Fig. S1 C) increased twofold, relative to controls, the total number of mCh-VAMP7$^+$ tubules that associated with melanosomes (Fig. 1, D and E, arrowheads; and Video 2, arrowheads; siMyo6, 8 ± 1.1; siCtrl; 4 ± 0.6). Among these tubules, the number that formed during a 40-s live acquisition was not statistically different in control and Myo6-depleted cells (Fig. S1 D). This indicates that the initiation or the emergence of melanosomal tubules was not affected by Myo6 depletion. Rather, the percentage of tubules that detached from melanosomes during the acquisition was threefold lower upon Myo6 depletion (Fig. 1, F–H; siCtrl, 32 ± 5.9%; siMyo6, 9.7 ± 0.5%). Importantly, in Myo6-depleted cells, the increased number of tubules and the defect in tubule release were both largely rescued by the reexpression of an siRNA-resistant full-length Myo6 fused to GFP (GFP-Myo6^R; Fig. 1, E and F). To determine whether Myo6 is present at the site of tubule release, we assessed the localization of full-length Myo6 fused to GFP (GFP-Myo6) relative to the mCh-VAMP7$^+$ melanosomal tubules. GFP-Myo6 decorated punctate structures associated with mCh-VAMP7$^+$ melanosomes (Fig. S1 E, arrows) from which the tubules emerged (Fig. S1 E, arrowheads). Its presence at the intersection between the melanosome core and its associated tubule (see also below) is consistent with a potential role for Myo6 during tubule fission and release. Of note, the dynamic release (Fig. S1 F, red arrow) of mCh-VAMP7$^+$ tubules (Fig. S1 F, arrowheads) from melanosomes occurred precisely at the GFP-Myo6$^+$ subdomains (Fig. S1 F, arrows; and Video 3). Together, these data indicate that Myo6 controls the fission and/or release of melanosomal recycling tubules.

To determine whether tubule release requires Myo6 motor function, we treated cells with 2,4,6-triiodophenol (TIP), a specific inhibitor of its ATPase activity (Heissler et al., 2012). Although TIP treatment did not alter Myo6 expression (Fig. S1 G), the number of mCh-VAMP7$^+$ tubules associated with melanosomes increased twofold as compared with treatment with vehicle (Fig. 1, I and J; and Video 4, arrowheads; DMSO, 2.7 ± 0.2 tubules; TIP, 5.3 ± 0.8 tubules) or with another drug as control, the myosin II inhibitor blebbistatin (Fig. S1 H; Straight et al., 2003; Limouze et al., 2004). Furthermore, TIP treatment dramatically

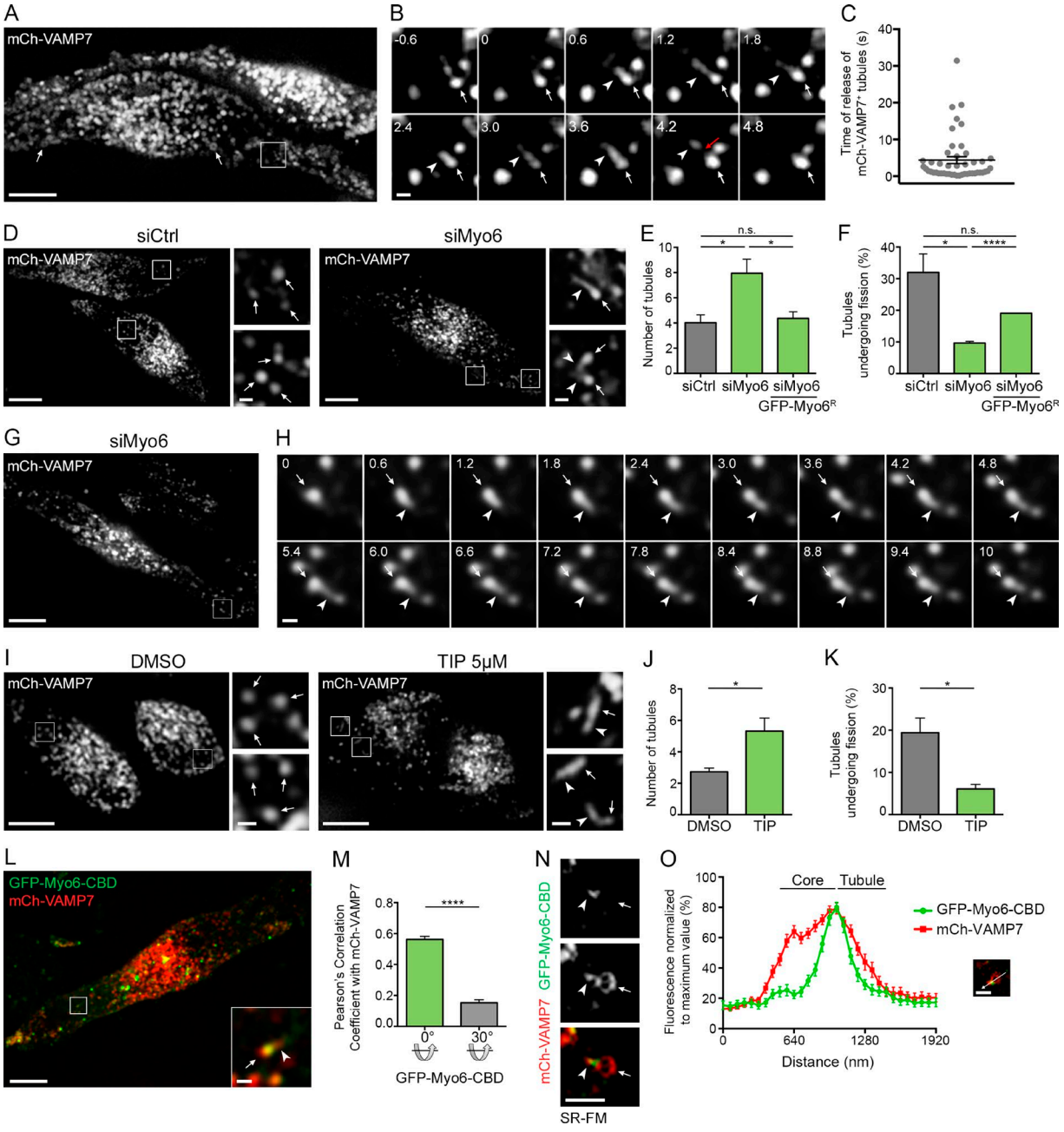

Figure 1. **Myo6 releases tubules from melanosome. (A and B)** Live imaging frames of mCh-VAMP7 expressing MNT-1 cells. VAMP7 localizes to melanosomes (A, arrows). Magnified views (B; 3× boxed area in A) of consecutive time-lapse images show VAMP7$^+$ tubule (arrowheads) emerging and detaching (red arrow) from melanosome (arrows) over time (s). **(C)** Quantification of the time of release of mCh-VAMP7$^+$ tubules from melanosomes (n = 4 independent experiments). **(D)** Live imaging frames of mCh-VAMP7 expressing siCtrl or siMyo6 MNT-1 cells. Magnifications (4×) of boxed area in siMyo6 cells show VAMP7$^+$ tubules (arrowheads) associated with melanosomes (arrows). **(E)** Relative number of mCh-VAMP7$^+$ melanosomal tubules during 40-s movies per 256-µm^2 area of cells treated with siCtrl or siMyo6 expressing or not GFP-Myo6^R (siCtrl, n = 4 independent experiments; siMyo6, n = 3 independent experiments; siMyo6+GFP-Myo6^R, n = 3 independent experiments). **(F)** Percentage of mCh-VAMP7$^+$ tubules detaching from melanosomes in cells treated as in E (E andF; siCtrl, n = 4 independent experiments; siMyo6, n = 3 independent experiments; siMyo6 + GFP-Myo6^R, n = 3 independent experiments). **(G and H)** Live imaging frames of mCh-VAMP7 expressing Myo6-depleted MNT-1 cells. Magnified views (H; 4× boxed area in G) depict VAMP7$^+$ tubule (arrowheads) emerging from a melanosome (arrows) without detaching over time (s). **(I)** Live cell imaging analysis of mCh-VAMP7 expressing MNT-1 cells treated with DMSO or 5 µM TIP. Magnified areas (4×) of boxed regions show tubules (arrowheads) associated with melanosomes (arrows). **(J)** Relative number of mCh-VAMP7$^+$ melanosomal tubules during 40-s movies per 256-µm^2 area of cells treated as in I (DMSO, n = 3 independent experiments; TIP, n = 3 independent experiments). **(K)** Percentage of mCh-VAMP7$^+$ tubules released from melanosomes in DMSO- or TIP-treated cells (J and K; DMSO, n = 3 independent experiments; TIP, n = 3 independent experiments). **(L)** Live imaging frame of GFP-Myo6-CBD and mCh-VAMP7 expressing MNT-1 cells. Magnified boxed areas (4×) show a VAMP7$^+$ tubule (arrowhead) associated with a GFP-Myo6-CBD$^+$ melanosome (arrow). **(M)** Pearson's correlation coefficient of cells (n = 26) as in L. Control values were obtained by 30° rotation of the GFP layer of the same images. **(N and O)** Live SR-FM of GFP-Myo6-CBD and mCh-VAMP7 expressing MNT-1 cells (N) and linear pixel values (normalized to maximal fluorescence) across double positive melanosomes associated with tubules (O). GFP-Myo6-CBD peak of fluorescence intersects the core of n melanosome (arrow) and the tubule (arrowhead; n = 30). Data are presented as the mean ± SEM. Bars: (A, D, G, I, and L) 10 µm; (B, H, N and magnifications in D, I, and L) 1 µm. ****, P < 0.0001; *, P < 0.05; n.s., not significant (unpaired t test).

reduced the fraction of tubules that detached from melanosomes over time (Fig. 1 K; DMSO, 19.4 ± 3.5%; TIP, 6.1 ± 1.1%) without affecting their formation (Fig. S1 I). As an alternative approach, we tested the effect of expressing the motorless Myo6 C-terminal cargo-binding domain (GFP-Myo6-CBD), which localizes to membranes (Aschenbrenner et al., 2003; Altman et al., 2004), including melanosomes (Loubéry et al., 2012), without binding to F-actin. As observed in Myo6-depleted or TIP-treated cells (Fig. 1, D and I), GFP-Myo6-CBD$^+$ melanosomes (arrow) exhibited mCh-VAMP7$^+$ tubules (arrowhead) that appeared stably associated with melanosomes over time (Fig. 1 L and Video 5, arrowheads), further suggesting that Myo6 activity on F-actin is required for tubule release. Similar to GFP-Myo6 (Fig. S1, E and F), GFP-Myo6-CBD localized to discrete puncta, many of which associated with mCh-VAMP7$^+$ (P = 0.56) or TYRP1-RFP$^+$ (P = 0.73) melanosomes (Fig. 1, L and M; and Fig. S1, J and K, arrowheads). In addition, using multifocal structured illumination superresolution fluorescence microscopy (SR-FM; Materials and methods; York et al., 2012), GFP-Myo6-CBD localized precisely on melanosomes to the core/tubule intersection (Fig. 1, N and O, arrow and arrowhead, respectively). Altogether, these data show that Myo6 motor activity promotes the fission and/or release of VAMP7-containing tubules from melanosomes.

Optineurin cooperates with Myo6 during the release of melanosomal tubules

We next assessed Myo6 localization in MNT-1 cells and normal human melanocytes (NHMs) using superresolution immunofluorescence microscopy (SR-IFM; Figs. 2 A and S2 A). As observed for GFP-Myo6 or GFP-Myo6-CBD (Fig. 1, L–O; Fig. S1, E, F, and J; and Fig. S2, B and C), endogenous Myo6 associated with discrete subdomains (Fig. 2, A and B; and Fig. S2 A, arrowheads) on nearly 90% of melanosomes labeled with TYRP1 (Fig. 2 C; 86 ± 2.1%). On average, each positive melanosome harbored approximately two Myo6 subdomains (Fig. 2 D; 1.82 ± 0.04).

Myo6 functions on different membranes together with specific adaptors (Tumbarello et al., 2013), among which optineurin associates with lysosomes and autophagosomes (Tumbarello et al., 2012; Sundaramoorthy et al., 2015). Like Myo6 (Fig. 2 A), endogenous optineurin is detected by SR-IFM on punctate structures (Fig. 2, E and F, arrowheads) that associated as subdomains with TYRP1$^+$ melanosomes in MNT-1 cells (Fig. 2 G; 79 ± 4.2%) or NHMs (Fig. S2 D, arrowheads). Consistently, optineurin associated with TYRP1$^+$ pigmented melanosome-enriched subcellular fractions of MNT-1 cells (Fig. S2 E, siCtrl, Mel lane). By SR-IFM, approximately two optineurin$^+$ puncta (1.87 ± 0.05) were detected per melanosome (Fig. 2 H) that partially overlapped with Myo6 (Fig. 2 I, arrowheads; Manders overlap coefficient = 0.4) on >80% of GFP-Myo6-CBD$^+$ melanosomes (Fig. 2 J, 85 ± 4.4%). Additionally, GFP-Myo6-CBD immunoprecipitate (IP) was enriched in optineurin relative to GFP-IP (Fig. 2 K), suggesting that optineurin and Myo6 associate with each other on melanosomal subdomains.

We further explored whether optineurin contributes to the recruitment and/or association of Myo6 with melanosomes. Depletion of optineurin in MNT-1 cells did not affect the association of Myo6 with melanosomes by subcellular fractionation (Fig. S2, E and F). Also by live imaging, GFP-Myo6-CBD localized as puncta associated with mCh-VAMP7$^+$ melanosomes in control- or optineurin-depleted cells (Fig. S2, G–I, arrowheads). Next, we addressed whether optineurin contributes to the release of melanosomal tubules. As in Myo6-depleted or TIP-treated cells, optineurin depletion in MNT-1 cells doubled the total number of mCh-VAMP7$^+$ tubules (arrowheads) associated with melanosomes (Fig. 2, L and M, arrows), without increasing the number of tubules that emerged from melanosomes during the acquisition (Fig. S2 J). This reflected a dramatic reduction in the number of tubules that detached from melanosomes over the time of acquisition (Fig. 2 N; siCtrl, 32 ± 5.9%; siOptn, 9.7 ± 0.4%). Although optineurin does not recruit Myo6, our data suggest collectively that it could control Myo6 activity to promote the efficient release of recycling tubules from melanosomes.

Myo6 constricts the neck of recycling melanosomal tubules

To establish how Myo6 controls the release of melanosomal tubules, we analyzed MNT-1 cells expressing GFP-Myo6-CBD by correlative light and electron microscopy (CLEM). Cells were immobilized by high-pressure freezing (HPF) to preserve membranes in their native state (Murk et al., 2003) and then processed for CLEM analysis (Materials and methods; Kukulski et al., 2011; Heiligenstein et al., 2014; Delevoye et al., 2016; Hurbain et al., 2017). Thick sections (300 nm) postlabeled with Hoechst dye (blue) to reveal nuclei were observed by wide-field fluorescence microscopy and screened for GFP (green)$^+$ structures associated with photon-dense pigmented melanosomes in bright field (Fig. 3 A, merge, boxed area, arrows). Low-magnification EM micrographs of cells of interest were acquired and overlaid to the light microscopy images (Paul-Gilloteaux et al., 2017; Fig. 3 B). Chosen areas consisting of GFP-Myo6-CBD$^+$ pigmented melanosomes (Fig. 3 B, boxed area) were processed by double-tilt 3D electron tomography to reveal their 3D ultrastructure (Fig. 3 C; Hurbain et al., 2008). The corresponding 3D model of one such area (Fig. 3 D and Video 6) showed a tubule (Fig. 3 D, arrowhead) in continuity with the limiting membrane of the melanosome (Fig. 3 D, arrow). Using eC-CLEM software (Paul-Gilloteaux et al., 2017), we estimated that the registration accuracy of the fluorescent signal within that area was 41 nm. This suggests that GFP-Myo6-CBD likely localizes to the neck of the tubule (Fig. 1, N and O), as predicted for a role for Myo6 in tubule fission.

To further characterize the ultrastructure of the melanosomal carriers, we performed conventional 2D-EM analyses of nontreated, control, and Myo6-depleted MNT-1 cells immobilized by HPF. While control cells harbored typical round or ovoid pigmented melanosomes (Fig. 3 E, arrows), Myo6-depleted cells contained numerous melanosomes with large tubular extensions (Fig. 3, E and F; and Fig. S3 A, arrowheads). Importantly, connected tubular extensions were also observed in siCtrl or nontreated cells (Figs. 3 F and S3 B, arrowheads), but at a much lower frequency than in Myo6-depleted cells (Fig. 3 G). In addition, quantification showed that the tubular structures in Myo6-depleted cells were longer (Fig. 3 H; siMyo6, 155 ± 4 nm; siCtrl, 124 ± 10 nm) and their necks were wider (Fig. 3 I; siMyo6, 143 ± 4; siCtrl, 114 ± 9 nm) than in control cells. Also, a plot of the distribution of the neck width showed that whereas highly constricted

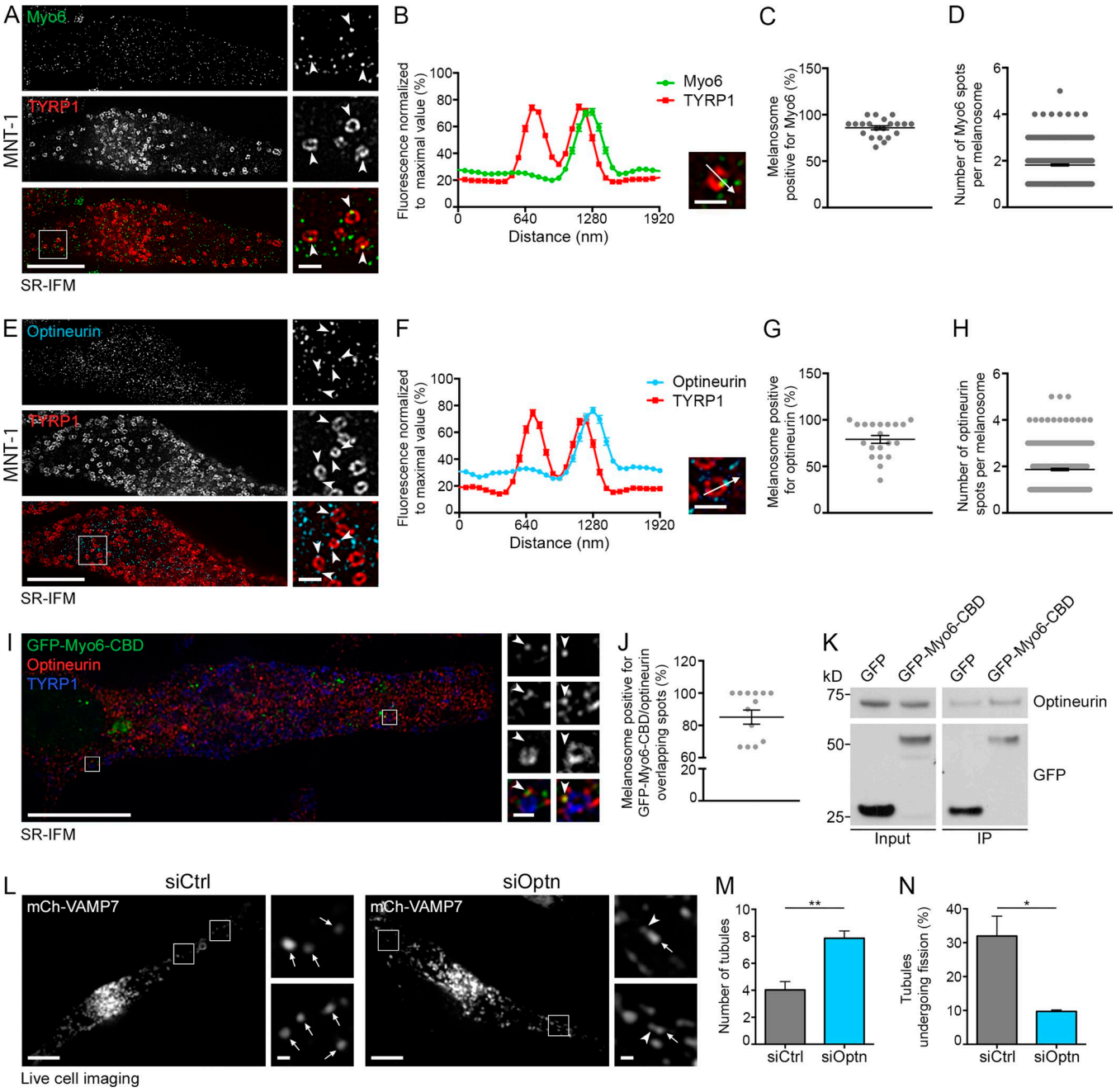

Figure 2. **Optineurin associates with Myo6 and releases melanosomal tubules. (A and B)** SR-IFM on MNT-1 cells costained for endogenous Myo6 and TYRP1 (A) and linear pixel values across n melanosomes (B; *n* = 130) show Myo6 (A; arrowheads, 4× boxed regions) localization to TYRP1⁺ melanosomal subdomain. **(C and D)** Percentage of Myo6/TYRP1⁺ melanosomes (C; *n* = 15 cells), and relative number of Myo6⁺ spots per *n* melanosome (D; *n* = 441). **(E and F)** SR-IFM of MNT-1 cells costained for endogenous optineurin and TYRP1 (E) and linear pixel values across n melanosomes (F; *n* = 95) show optineurin (E; arrowheads, 4× boxed regions) localization to TYRP1⁺ melanosomal subdomain. **(G and H)** Percentage of optineurin/TYRP1⁺ melanosomes (G; *n* = 20 cells) and relative number of optineurin⁺ spots per *n* melanosome (H; *n* = 400). **(I)** SR-IFM on GFP-Myo6-CBD–expressing MNT-1 cells labeled for optineurin and TYRP1. Magnified views (4×) show Myo6 and optineurin codistribution on TYRP1⁺ melanosome subdomains. **(J)** Quantification of the percentage of melanosomes with overlapping GFP-Myo6-CBD and optineurin subdomains as in I (*n* = 14 cells). **(K)** Western blot analysis of lysates and GFP IPs of GFP- or GFP-Myo6-CBD–expressing MNT-1 cells probed for optineurin or GFP antibodies. **(L)** Live imaging frames of MNT-1 cells expressing mCh-VAMP7 and treated with control or optineurin (Optn) siRNAs. Magnified areas (4×) of boxed regions in siOptn cells show tubules (arrowheads) associated with melanosomes (arrows). **(M)** Relative number of mCh-VAMP7⁺ melanosomal tubules during 40-s movies per 256-µm² area of cells treated as in L (siCtrl, *n* = 4 independent experiments; siOptn, *n* = 3 independent experiments). **(N)** Percentage of mCh-VAMP7⁺ tubules detaching from melanosomes in control- or optineurin-depleted cells (M and N; siCtrl, *n* = 4 independent experiments; siOptn, *n* = 3 independent experiments). Molecular masses are in kilodaltons. Data are presented as the mean ± SEM. Bars: (A, E, I, and L) 10 µm; (A, B, E, F, and L, magnifications) 1 µm; (I, magnifications) 500 nm. **, P < 0.01; *, P < 0.05 (unpaired *t* test).

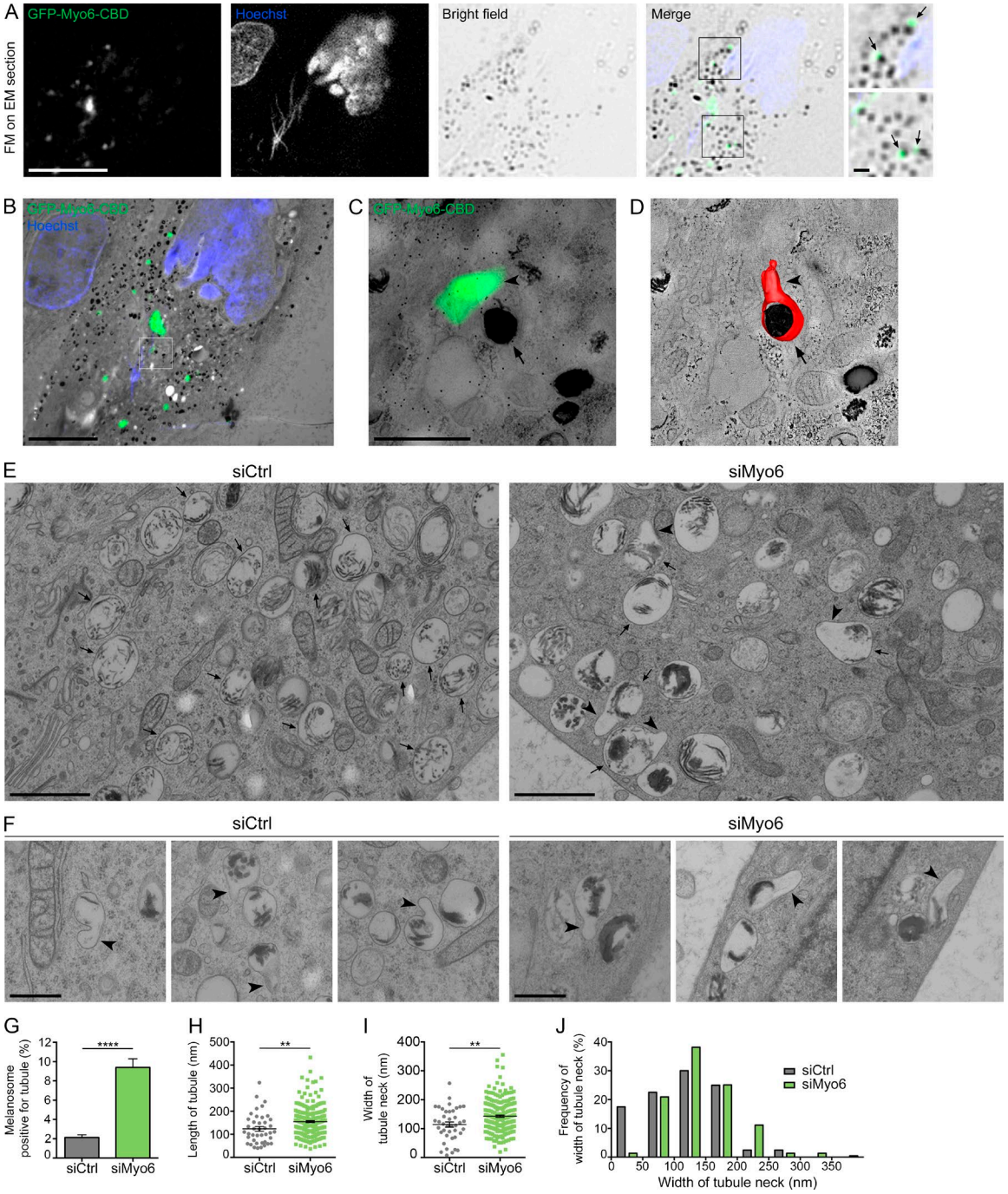

Figure 3. **Myo6 constricts the neck of melanosomal tubules. (A)** FM focal projection from a 300-nm-thick EM section from a high-pressure frozen MNT1 cell expressing GFP-Myo6-CBD. GFP-Myo6-CBD (green) was preserved during freeze substitution. Nuclei (blue) were poststained with Hoechst (blue stripes outside the nucleus correspond to folds in the EM section). Black melanin pigment was imaged in bright field. Magnified area (2×) of the merged channels reveal GFP signals adjacent to melanosomes (arrows) that is comparable to that seen in live-cell imaging observations (Fig. 1 L). **(B)** FM and EM images of the section are registered and overlaid to identify GFP-Myo6-CBD$^+$ pigmented melanosome (boxed area). **(C)** Zero-tilt image of the tomogram registered and overlaid with GFP-Myo6-CBD fluorescent signal. **(D)** Manually contoured 3D model shows the melanosomal membrane (red, arrow) filled with black melanin pigment and in continuity with an elongated tubule (arrowhead). **(E)** 70-nm electron micrograph from control- or Myo6-depleted MNT-1 cells. Upon siMyo6 treatment, large tubules (arrowheads) are connected and emanate from melanosomes (arrows). **(F)** Gallery of melanosomal tubules (arrowheads) associated with melanosomes in control- or Myo6-depleted cells. **(G)** Percentage of melanosomes positive for tubule per *n* cell on EM section (siCtrl, *n* = 27; siMyo6, *n* = 23). **(H and I)** Mean length of n tubules (H) and width of the neck (I) measured in cells treated as in E (siCtrl, *n* = 41; siMyo6, *n* = 215). **(J)** Distribution of the width of tubules neck. Data are presented as the mean ± SEM. Bars: (A and B) 10 µm; (C, E, F, and magnifications in A) 1 µm. ****, P < 0.0001; **, P < 0.01 (unpaired *t* test).

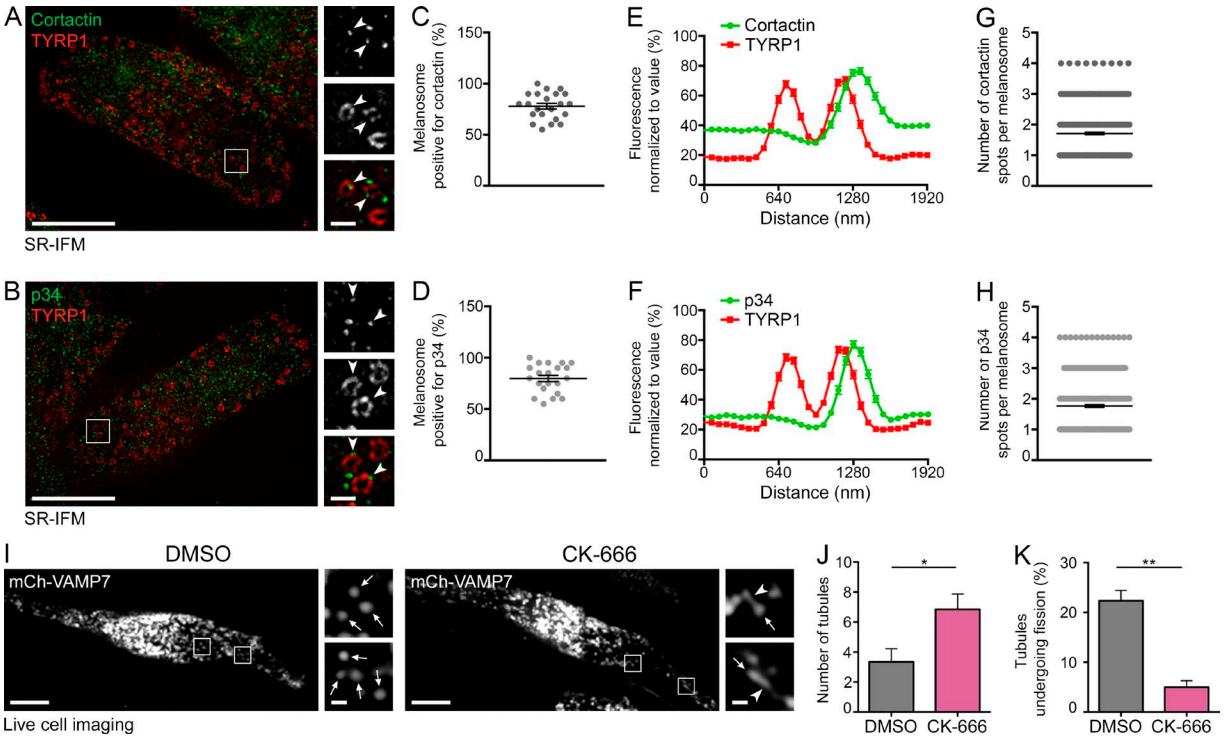

Figure 4. **Fission of melanosomal tubules requires the Arp2/3 complex activity. (A and B)** SR-IFM on MNT-1 cells costained for endogenous cortactin (A) or p34 (B) and TYRP1. Cortactin and p34 (A and B; arrowheads, 3× of boxed regions) localize as discrete puncta associated with TYRP1⁺ melanosomes. **(C and D)** Percentage of TYRP1⁺ melanosomes positive for cortactin (C) or p34 (D). **(E and F)** Linear pixel values across n melanosomes show cortactin (E) or p34 (F) fluorescence enrichment at TYRP1⁺ melanosomal subdomain (cortactin, n = 102; p34, n = 94). **(G and H)** Relative number of cortactin (G) and p34 (H) fluorescent spots per n melanosome (C, D, G, and H; cortactin, n = 441; p34, n = 420). **(I)** Live imaging frame of mCh-VAMP7 expressing MNT-1 treated with DMSO or 50 µM CK-666. Magnified areas (4×) of boxed regions show tubules (arrowheads) associated with melanosomes (arrows). **(J)** Relative number (n) of mCh-VAMP7⁺ melanosomal tubules during 40-s movies per 256-µm² area of cells treated as in I (DMSO, n = 5 independent experiments; CK-666, n = 3 independent experiments). **(K)** Percentage of mCh-VAMP7⁺ tubules detaching from melanosomes in DMSO- or CK-666–treated cells (J and K; DMSO, n = 5 independent experiments; CK-666, n = 3 independent experiments). Data are presented as the mean ± SEM. Bars: (A, B, and I) 10 µm; (A, B, and I, magnifications) 1 µm. **, P < 0.01; *, P < 0.05 (unpaired t test).

tubules (<50 nm width) constituted ~20% of tubules in control cells, they were barely represented in Myo6-depleted cells (Fig. 3 J). EM analyses of cells treated with TIP showed similar wide-necked tubules (Fig. S3, C and D, arrowheads), indicating that Myo6 motor activity is required for constriction of melanosomal tubules.

Melanin polymerizes on elongated and rigid amyloid fibrillary sheets that deform melanosomes to their ovoid shape (Bissig et al., 2016). We reasoned that melanized sheets might enter the lumen of the enlarged tubules of Myo6-depleted cells and provide a rigid internal scaffold to prevent their constriction. However, in any tested condition, we rarely observed melanin⁺ sheets within tubules, suggesting that they are actually excluded from the recycling melanosomal tubules (Fig. 3, E and F; and Fig. S3, A–D). Moreover, the tubules in control or Myo6-depleted cells often oriented parallel to the long axis of the polymerized sheets (Fig. S3, E and F). This suggests that the inherent mechanical properties of melanin⁺ fibrillary sheets might define the site of tubule formation and Myo6-driven fission.

Arp2/3-mediated actin nucleation supports melanosomal tubule fission

Given that Myo6 is an actin-based motor and that branched F-actin plays an important role in endosomal membrane dynamics (Gautreau et al., 2014), we assessed the role of F-actin and Arp2/3 in melanosomal tubule fission. We first asked whether branched F-actin or the Arp2/3 complex could be detected by SR-IFM in proximity to melanosomes. We labeled cells with antibodies to the p34 subunit of the Arp2/3 complex or to endogenous cortactin, a class II nucleation-promoting factor that interacts and codistributes with Arp2/3 and used here as a branched F-actin reporter (Schnoor et al., 2018). Both cortactin (78 ± 2.8%) and p34 (79.8 ± 3%) associated with a majority of TYRP1⁺ melanosomes (Fig. 4, A–F, arrowheads), and they decorated approximately two subdomains per melanosome (Fig. 4, E–H; cortactin, 1.7 ± 0.04; p34, 1.7 ± 0.05) that codistributed with Myo6 (Fig. S4, A–D, arrowheads).

We next tested whether Arp2/3 activity is required for tubule formation using CK-666 (Nolen et al., 2009), a small-molecule inhibitor of Arp2/3 activity that stabilizes the complex in its inactive state and thus prevents the nucleation of branched F-actin (Hetrick et al., 2013). Similar to TIP-treated cells or to the depletion of Myo6 or optineurin, treatment of mCh-VAMP7–expressing MNT-1 cells with CK-666 increased twofold the number of mCh-VAMP7⁺ tubules (Fig. 4, I and J, arrowheads; DMSO, 3.3 ± 0.9; CK-666, 6.9 ± 1.0) associated with melanosomes (Fig. 4 I and Video 7, arrows). Also, the percentage of tubules that detach over time was reduced (Fig. 4 K), with no effect on the rate of

new tubules emerging from melanosome (Fig. S4 E). In contrast, tubule formation in cells treated with an inhibitor of formin-mediated actin polymerization, SMIFH2 (Rizvi et al., 2009), was comparable to that in the vehicle-treated controls (Fig. S4 F). Moreover, CK-666 treatment did not alter Myo6 expression or localization to melanosomes (Fig. S4, G and H, arrowheads). These data show that Arp2/3-dependent nucleation of branched F-actin contributes to the fission of melanosomal tubules.

The WASH complex contributes to the constriction and fission of melanosomal tubules

The WASH complex is another actin nucleation–promoting factor that contributes to the fission of endosomal tubular carriers by activating Arp2/3 and promoting local branched F-actin nucleation (Derivery et al., 2009; Gomez and Billadeau, 2009). Using SR-IFM, nearly 70% of TYRP1$^+$ melanosomes associated with the WASH1 subunit (Fig. S4 I; 67.4 ± 3.5%) that similarly decorated approximately two subdomains per melanosome (Fig. S4 J; 1.6 ± 0.04). These subdomains partially overlapped with F-actin (labeled by cortactin; Fig. S4, K and L, arrowheads) or with Myo6 (Fig. S4, M and N, arrowheads; Manders overlap coefficient = 0.33) on >50% of GFP-Myo6-CBD$^+$ melanosomes. Interestingly, anti-GFP coimmunoprecipitation assays on transfected MNT-1 cell lysates showed that the WASH complex subunit strumpellin, but not WASH1, was enriched in GFP-Myo6-CBD IPs compared with the GFP control. As a positive control, both subunits were highly enriched in IPs from cells expressing GFP-Vps35, a subunit of the retromer complex that interacts directly with the WASH complex (Harbour et al., 2012; Fig. S4 O). Therefore, this suggests together that a fraction of Myo6 associates weakly and/or transiently with the WASH complex to melanosomes.

In addition, and as observed for Myo6 depletion or Arp2/3 inhibition, destabilization of the WASH complex by depletion of WASH1 (Derivery et al., 2009; Fig. S4 P) increased the percentage of melanosomes that associated with mCh-VAMP7$^+$ tubules relative to control without affecting their formation (Fig. 5, A and B; Fig. S4 Q; and Video 8). Importantly, the proportion of tubules undergoing fission in WASH1-depleted cells decreased relative to control (Fig. 5 C). Conventional 2D-EM analysis of high-pressure frozen WASH1-depleted MNT-1 cells revealed numerous tubular extensions in continuity with the limiting melanosomal membrane (Figs. 5 D and S4 R, arrowheads), as observed in Myo6-depleted cells (Fig. 3). Similarly, these tubular extensions were more abundant and longer and their necks were wider than those in control cells (Fig. 5, E–G; length, siWASH1: 157 ± 6 nm and siCtrl: 124 ± 10 nm; width, siWASH1: 157 ± 5 nm and siCtrl: 114 ± 9 nm). Finally, tubules with a constricted neck (<50 nm) were barely detected (Fig. 5 H). Our data show that WASH depletion recapitulates the phenotype of Myo6-depleted melanocytes and support a model in which Myo6 and WASH-mediated actin polymerization cooperate to constrict the melanosomal tubule before fission.

Myo6, WASH, and optineurin are required for melanosome homeostasis and function

We have previously shown that depleting Myo6 in melanocytes led to increased melanin content and the accumulation of TYRP1 on melanosomal membranes by immuno-EM (IEM; Loubéry et al., 2012). To validate and extend this result, we first confirmed that Myo6-, WASH1-, and optineurin-depleted cells (Figs. 6 A and S5 A) had increased melanin pigment content (Figs. 6 B and S5 B; siMyo6, 1.21 ± 0.05; siWASH1, 1.13 ± 0.03; siOptn, 1.21 ± 0.08 and normalized to siCtrl). Consistently, depletion of Myo6, WASH1, or optineurin increased the amount of TYRP1 and also VAMP7 detected in melanosomal subcellular fractions (Fig. 6, C and D; and Fig. S5, C and D), indicating that increased melanin content correlates with increased melanosomal cargo content. IEM analysis showed that depletion of Myo6 or WASH1 increased the percentage of GFP-VAMP7$^+$ pigmented melanosomes as well as the number of GFP-VAMP7–associated gold particles (Fig. 6 E, arrowheads) per melanosome (Fig. 6, E–G). These data suggest that the homeostasis of melanosomes is perturbed after depletion of Myo6, WASH1 or optineurin. To investigate alteration in homeostasis, we monitored the luminal pH of melanosomes by incubating control- or Myo6-depleted cells with the weak base 3-(2,4-dinitroanilino)-3′-amino-*N*-methyldipropylamine (DAMP), which accumulates and labels acidic compartments (Anderson et al., 1984; Raposo et al., 2001). Myo6 depletion resulted in increased DAMP codistribution with TYRP1 by IFM (Fig. S5 E, arrowheads) and increased DAMP labeling within pigmented melanosomes by IEM (Fig. S5, F and G, arrowheads), indicating acidification of the melanosomal lumen. Together, these data indicate that the Myo6-, WASH-, and optineurin-driven fission of recycling tubules is necessary to maintain the homeostasis of melanosomes.

Given that organelle homeostasis is tightly linked to organelle function, we investigated if depleting Myo6 affects melanosome physiology. In skin, melanosomes support two critical tasks regarding pigmentation: (1) the synthesis and storage of melanin pigments within melanocytes and (2) the dispersion of melanin pigments throughout the epidermis after secretion and transfer to neighboring keratinocytes (Delevoye, 2014). As Myo6 depletion resulted in increased intracellular melanin content (Fig. 6 B), we examined whether pigment release was affected. We first quantified melanin release into the medium by control- or Myo6-depleted MNT-1 cells treated with forskolin, a permeable activator of adenylyl cyclase that raises cAMP levels in melanocytes, and thus stimulates their pigmentation and secretion capacities (Brenner and Hearing, 2008), and observed a 32 ± 8% decrease in pigment secretion upon Myo6 depletion (Fig. 6 H). Then, using control-, Myo6-, WASH1-, or optineurin-depleted NHMs (Fig. S5 H) co-cultured with normal human keratinocytes (NHKs), we evaluated the melanin transfer by IFM analysis (Fig. 6 I and S5 I; using labeling for amyloid fibrils with HMB45 antibody; see Materials and methods; Singh et al., 2008). Depletion of any of these components in NHMs decreased the frequency of HMB45$^+$ NHKs (Fig. 6 J; siCtrl, 83 ± 5%; siMyo6, 60 ± 1%; siWASH1, 71 ± 3%; siOptn, 64 ± 1%), and the co-cultured NHKs also harbored less melanin fluorescent signal than NHKs co-cultured with siCtrl-treated NHMs (Fig. 6 K). Thus, the Myo6-, WASH-, and optineurin-driven fission of recycling melanosomal tubules impacts the fate of melanosomes likely by regulating their homeostasis and function.

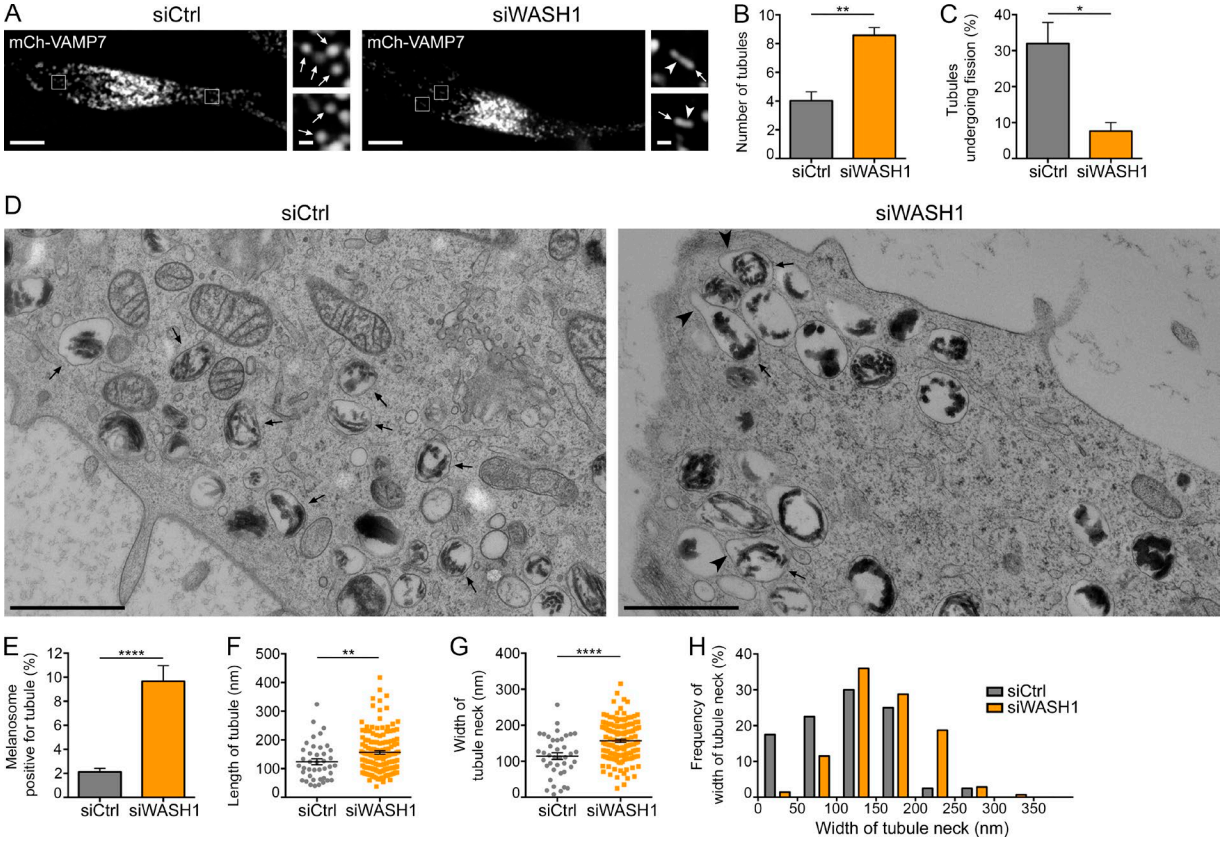

Figure 5. **The WASH complex promotes melanosomal tubules constriction and fission. (A)** Live imaging frames on mCh-VAMP7 expressing MNT-1 cells treated with control or WASH1 siRNAs. Magnified areas (4×) of boxed regions show tubules (arrowheads) associated with melanosomes (arrows). **(B and C)** Relative number of mCh-VAMP7$^+$ melanosomal tubules (B) detaching from melanosomes (C) during 40-s acquisition per 256-µm^2 area of cells treated as in A (siCtrl, *n* = 4 independent experiments; siWASH1, *n* = 3 independent experiments). **(D)** High-pressure frozen control- or WASH1-depleted MNT-1 cells analyzed by 2D EM. Large tubules (arrowheads) emerge from melanosomes (arrows) upon siWASH1 treatment. **(E)** Percentage of melanosomes positive for tubule per n cell on EM section (siCtrl, *n* = 27; siWASH1, *n* = 21). **(F and G)** Mean length (F) of n tubules and width (G) of the neck (siCtrl, *n* = 41; siWASH1, *n* = 139). **(H)** Frequency of distribution of the width of tubules neck. Data are presented as the mean ± SEM. Bars: (A) 10 µm; (D and magnifications in A) 1 µm. ****, P < 0.0001; **, P < 0.01; *, P < 0.05 (unpaired *t* test).

Discussion

To maintain their identity and function, intracellular organelles constantly receive and export contents through membranous transport intermediates. Myosins and/or actin dynamics have been implicated in fission events at endosomes (Derivery et al., 2009), mitochondria (De Vos et al., 2005), the TGN (Miserey-Lenkei et al., 2010), and the plasma membrane during endocytosis (Ferguson et al., 2009; Römer et al., 2010; Taylor et al., 2012), but whether they remodel the membrane to promote severing is not known. Here, we report that the constriction and fission of tubules from melanosomes for cargo retrieval is mediated by Myo6 activity in collaboration with optineurin and WASH- and Arp2/3-dependent actin nucleation. By releasing transport intermediates from melanosomes loaded with specific components, Myo6-driven fission tunes the content, maturation, and ultimately secretion of melanosomes.

Myo6 is a multitasking motor that can move organelles or vesicles along actin tracks or tether them to the cytoskeleton (Altman et al., 2004). In melanocytes, Myo6 does not appear to facilitate melanosome movement but rather likely organizes and/or stabilizes F-actin (Loubéry et al., 2012). Our data show that Myo6 codistributes with branched F-actin at melanosomal subdomains, suggesting that Myo6 can cross-link the melanosome to F-actin through its CBD and motor domain, respectively. Our CLEM and SR-IFM data suggest that Myo6 localizes most likely to the neck of emerging melanosomal tubules. Also, our functional data show that tubule constriction and fission are impaired by Myo6 depletion, inhibition of its motor activity, or expression of a motorless form. A mechanism for membrane fission named friction-driven scission has been recently proposed (Simunovic et al., 2017) and relies on the frictional forces generated by proteins at the neck of elongated tubules, which can then conduct their fission. Thus, by exerting forces on the actin network at the base of an elongated structure, Myo6 is ideally placed to constrict melanosomal tubules and to lead to their fission and release.

Why would Myo6 and branched F-actin be specifically required for tubule constriction? In mammals (and in contrast to yeast; Liu et al., 2006; Aghamohammadzadeh and Ayscough, 2009), actin is dispensable during clathrin-mediated endocytosis (CME), except when cells internalize large particles, like pathogens (Cureton et al., 2009), or when the plasma membrane is highly rigid (Aghamohammadzadeh and Ayscough, 2009; Boulant et al., 2011), as suggested for the apical plasma membrane in polarized cells (Boulant et al., 2011). Similarly, Myo6

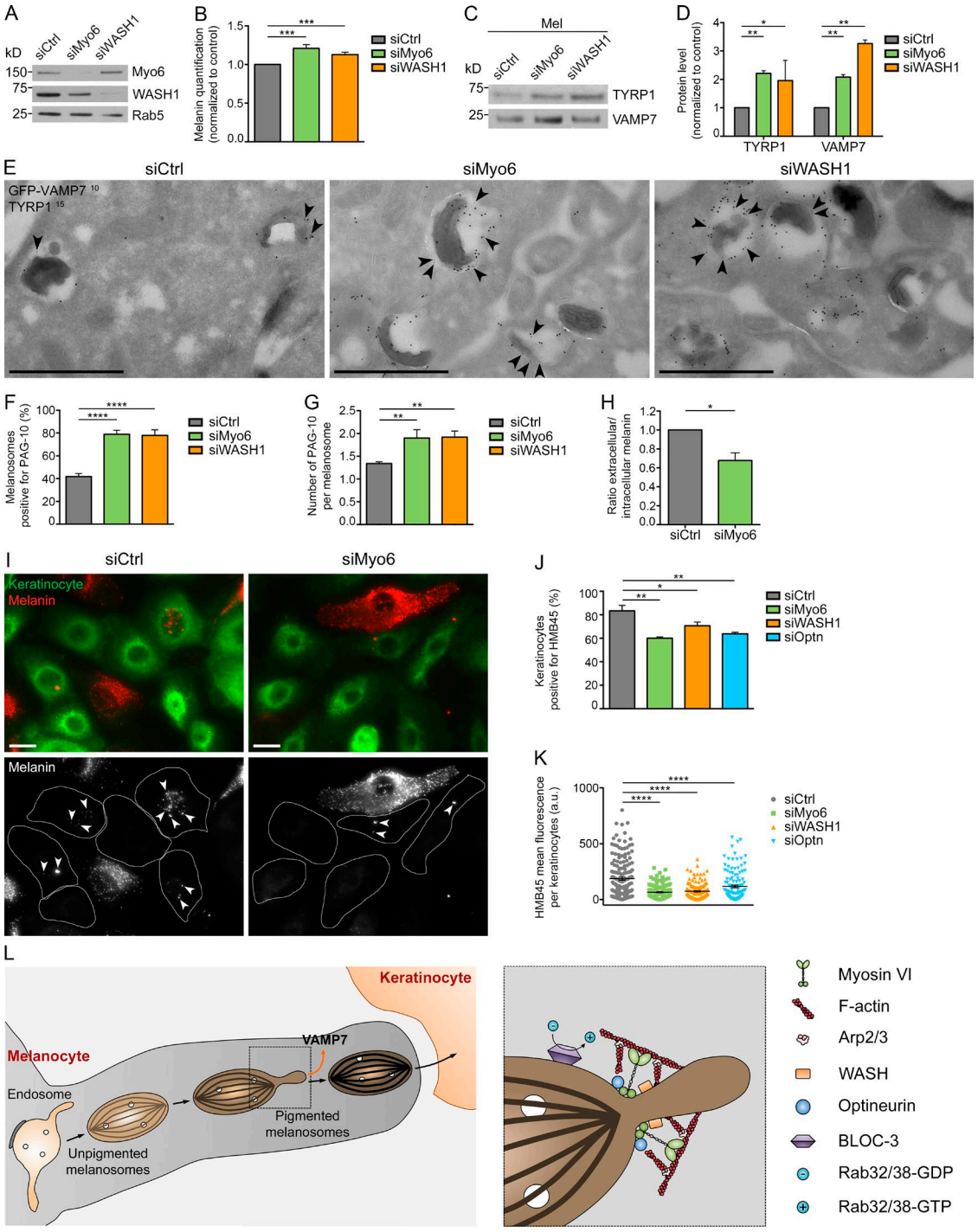

Figure 6. **Melanin production, cargo export, melanosome secretion, and transfer rely on Myo6, WASH, or optineurin. (A)** Western blot of total lysates of control-, Myo6-, or WASH1-depleted MNT-1 cells probed with respective antibodies. **(B)** Intracellular melanin estimation of control-, Myo6-, or WASH1-depleted MNT-1 cells ($n = 8$ independent experiments; normalized to control). **(C)** Western blot of melanosome-enriched (Mel) fractions from control-, Myo6-, or WASH1-depleted MNT-1 cells probed with respective antibodies. **(D)** Quantification of TYRP1 and VAMP7 protein expression levels on Mel fractions in C and normalized to control ($n = 2$ independent experiments). **(E)** GFP-VAMP7–expressing MNT-1 cells treated with siCtrl, siMyo6, or siWASH1 were processed for ultrathin cryosectioning and double immunogold labeled for GFP (PAG 10 nm, arrowheads) and TYRP1 (PAG 15 nm). **(F and G)** Percentage of GFP-VAMP7$^+$ melanosome per n cell on section (F) and relative number of gold particles per GFP-VAMP7$^+$ melanosome (G; siCtrl, $n = 7$; siMyo6, $n = 6$; siWASH1, $n = 7$). **(H)** Ratio of extracellular to intracellular melanin content of control-, Myo6-, or WASH1-depleted MNT-1 cells treated with 30 µM forskolin ($n = 3$ independent experiments; normalized to control). **(I)** NHMs treated with control or Myo6 siRNAs were co-cultured with NHKs. Staining for HMB45 (red) or EGFR (green) identify melanin and NHM or NHK respectively. HMB45 staining within NHK (arrowheads) correspond to secreted and transferred melanin. **(J and K)** Quantification of the percentage of NHKs positive for at least one HMB45$^+$ spot (J; $n = 3$ independent experiments) and of the mean HMB45 intensity per stained (n) NHK (K) when co-cultured with siCtrl, siMyo6, siWASH1 or siOptn NHM (siCtrl, $n = 167$; siMyo6, $n = 147$; siWASH1, $n = 148$; siOptn, $n = 123$). **(L)** Working model illustrating the roles of Myo6, optineurin, F-actin, WASH, Arp2/3, and BLOC-3 complexes in the recycling pathway from melanosomes. Molecular mass is in kilodaltons. Data are presented as the mean ± SEM. Bars: (E) 1 µm; (I) 10 µm. ****, $P < 0.0001$; ***, $P < 0.001$; **, $P < 0.01$; *, $P < 0.05$ (unpaired t test in B, D, F, G, and H; multiple comparisons ordinary one-way ANOVA in J and K).

functions during the internalization of some bacteria (Bonazzi et al., 2011; Brooks et al., 2017) and in CME, specifically at the apical membrane of polarized cells (Buss et al., 2001), where tension is twofold higher than at the basolateral membrane (Boulant et al., 2011). Myo6 and F-actin might thus function in the remodeling of membranes with a large size and/or rigidity. Pigmented melanosome are 0.5 µm in length and filled with melanin polymer on a rigid amyloid matrix. Such a matrix might create an internal pressure imposing high stiffness to its limiting membrane that would be then difficult to remodel. The melanosomal tubules are unusually large compared with endosomal tubules and orient along the long axis of melanin-laden amyloid fibrils, suggesting that the membrane may be more deformable at the poles of the melanosome. Thus, Myo6 and actin might be required to exert high forces on a rigid membrane to complete tubule constriction, scission, and release.

The WASH complex promotes the Arp2/3-dependent actin polymerization on early endosomes to facilitate the release of recycling tubular intermediates in most cell types (Derivery et al., 2009; Gomez and Billadeau, 2009). In melanocytes, the WASH complex can be recruited to early endosomes (Tyrrell et al., 2016) but does not participate in the anterograde delivery of cargoes from endosomes to melanosomes (Delevoye et al., 2016; Ripoll et al., 2016). Consistently, gene targeting of the WASH complex subunit strumpellin in mice does not lead to hypopigmentation (Tyrrell et al., 2016). Interestingly, we show that Myo6 could interact with strumpellin in melanocytes. Also, the WASH complex associates with melanosomes and cooperates with Myo6 during the constriction and fission of recycling melanosomal tubules. Therefore, this might suggest that two coexisting WASH complexes can function in melanocytes to distinct organelles of endocytic origins, such as early endosomes and melanosomes.

Proper cargo sorting from endomembranes (Au et al., 2007; Chibalina et al., 2007; Carnell et al., 2011; King et al., 2013; Seaman et al., 2013; Buckley et al., 2016) and homeostatic regulation of lysosome and autophagosome size (Chibalina et al., 2007; Derivery et al., 2012; Duleh and Welch, 2012; Tumbarello et al., 2012) require branched F-actin polymerization, WASH activity, or Myo6 expression. Indeed, our previous study showed that melanosomes from Myo6 knockout mice are enlarged and hyperpigmented (Loubéry et al., 2012). This likely reflects, at least in part, the enrichment of components such as TYRP1 and VAMP7 and the failure to retrieve membrane via tubulation. The latter is consistent with studies showing that WASH or Myo6 depletion leads to enlarged endosomes devoid of tubules (Chibalina et al., 2007; Gomez et al., 2012). We hypothesize that a primary defect in membrane fission might secondarily result in cargo missorting leading to loss of organelle homeostasis and increased organelle size. Such aberrant organelles might ultimately be unable to recruit the machinery required for tubule initiation, perhaps explaining the defects in endosomal tubule formation observed in other cell types depleted of Myo6 or impaired for F-actin polymerization.

Skin pigmentation and photoprotection depend on the transfer of pigmented melanosomes from melanocytes to keratinocytes (Delevoye, 2014; Wu and Hammer, 2014). Here, we reveal a novel maturation step for melanosomes that impacts their extracellular release. Given that Arp2/3, Myo6, and optineurin control the docking and/or pore opening of secretory vesicles fusing with plasma membrane (Gasman et al., 2004; Bond et al., 2011; Tran et al., 2015), it was conceivable that they might play a direct role during melanosome secretion in melanocytes. However, neither excessive melanosomes association with the plasma membrane nor unresolved fusion profiles were observed at the ultrastructural level in cells with Myo6 or WASH depletion, making their direct involvement in melanosome secretion unlikely. Rather, the data support the conclusion that exporting components from melanosomes is required before their maturation and secretion.

How might recycling from melanosomes affect their secretion? In addition to cargoes and melanin accumulation, we show that impairing the Myo6-driven export pathway lowers the intraluminal pH of pigmented melanosomes. In melanocytes, neutralization of acidic early stage melanosomes by transporter such as OCA2 is required for melanization (Bellono et al., 2014). Consequently, mature pigmented melanosomes become neutral (Raposo et al., 2001) and competent for secretion. Interestingly in *Dictyostellium discoideum*, lysosomes destined for exocytosis alkalinize their lumen through a WASH- and Arp2/3-dependent retrieval of cargoes, including the vacuolar ATPase (Carnell et al., 2011; King et al., 2013; Thomason et al., 2017). The export of vacuolar ATPase, which associates with melanosomes (Tabata et al., 2008), might serve to raise the pH of melanosomes and promote their secretion. Other ion pumps and/or channels might also and nonexclusively follow this export route, such as the two-pore channel 2 that has been shown to regulate melanosome size, pH, and pigmentation (Ambrosio et al., 2016; Bellono et al., 2016; Patwardhan and Delevoye, 2016).

Whether Myo6 cooperates with other motors during membrane constriction from melanosomes is not known. The microtubule and actin cytoskeletons aid the formation, elongation, and scission of tubular recycling intermediates from endosomes (Delevoye et al., 2016). Similarly, the extension and delivery of melanosomal tubules to their target membranes likely requires microtubules and the pulling force exerted by kinesins or dynein. Moreover, additional myosins might cooperate with Myo6 to provide sufficient force for tubule fission from melanosomes. Interestingly during CME, type I myosins like the mammalian myosin 1E contributes, together with Arp2/3 and F-actin, to the internalization of cargo molecules (Krendel et al., 2007; Cheng et al., 2012), perhaps by constricting the neck of the endocytic vesicles before scission as illustrated in yeast (Idrissi et al., 2012). For instance in melanocytes, myosin Vc has been also proposed to regulate both melanosome cargo composition and melanosome secretion (Bultema et al., 2014). Whether these myosins might operate at a similar step as Myo6 remains to be explored.

The melanosomal tubules described here are very likely the same as those that we previously characterized to retrieve VAMP7 from melanosomes in mouse melanocytes (Dennis et al., 2016). Those require for their formation the biogenesis of LRO complex-3 (BLOC-3; Dennis et al., 2016), a guanine nucleotide exchange factor for the cell type–specific RAB GTPases RAB32 and RAB38 (Gerondopoulos et al., 2012). Indeed, we previously showed that GFP-RAB38 and its effector, VARP, localize to one

subdomain on melanosomes from which the tubules emerged (Dennis et al., 2016). Interestingly, Myo6, optineurin, WASH and branched F-actin decorate around two subdomains on melanosomes. Some of them that label for optineurin or WASH do not contain Myo6, suggesting that not all subdomains are productive 'hot-spots' for releasing tubules. The molecular details controlling local Myo6 recruitment and/or activity at the melanosome are not totally understood. However, whereas optineurin does not actively contribute to Myo6 recruitment, it likely regulates its activity. Therefore, it would be interesting to determine if RAB32, RAB38 and/or VARP play a role in positioning Myo6 and/or its partners for the fission of melanosomal tubule.

Thus, our data lead us to propose the following model (Fig. 6 L) in which Myo6 is precisely positioned at the neck of emerging melanosomal tubules, formed after the activation of RAB38 and/or RAB32 on melanosomes by BLOC-3. The WASH complex then directly activates locally the Arp2/3-mediated branched actin nucleation on melanosomes, allowing Myo6 to cross-link F-actin at the neck. Myo6 activity here might be positively regulated by optineurin and produces the necessary force to constrict and promote the fission and release of the tubule. The released tubules recycle VAMP7 for its possible reuse (Dennis et al., 2016) and likely also export additional components to allow for further melanosome maturation. We propose that such maturation may be required for late events in melanosome biology, including transfer to keratinocytes.

Altogether, our current work identifies a new function for Myo6 and branched F-actin in the constriction of membranes, leading to the fission and release of transport carriers required for the function of organelles. Understanding if Myo6 can similarly remodel membranes others than at melanosomes, how membrane rigidity could impact Myo6 function, and whether such constricting activity might be targeted in diseases deserve further scrutiny in future studies.

Materials and methods

Cell culture and transfections

MNT-1 cells were cultured in DMEM supplemented with 20% FBS, 10% AIM-V medium, sodium pyruvate, nonessential amino acids, and penicillin-streptomycin (Gibco). Human foreskin neonatal melanocytes (NHMs) and keratinocytes (NHKs) were obtained from Cellsystems. NHMs were cultured in DermaLife Basal Medium supplemented with DermaLife M Life Factors and NHK in DermaLife Basal Medium with DermaLife K Life Factors (Lo Cicero et al., 2015). For plasmid transfection, MNT-1 cells were seeded at day 1, transfected with 2 µg plasmids using Lipofectamine 2000 (Thermo Fisher Scientific) at day 3, and analyzed at day 4. For siRNAs, MNT-1 cells were seeded at day 1, transfected with siRNAs (200 pmol) using Oligofectamine (Thermo Fisher Scientific) at day 3, collected and analyzed at day 6 (for imaging experiments), or transfected again at day 5 and analyzed at day 8 (for biochemical analyses). For live-cell imaging, MNT-1 cells were cultured at day 1, treated with siRNAs at day 3, transfected with plasmids at day 5, and analyzed at day 6.

Antibodies

The antibodies used were as follows: rabbit anti–Myo6 (1:1,000 Western blot [WB], 1:200 immunofluorescence [IF]; a gift from F. Buss, Cambridge Institute of Medical Research, Cambridge, England, UK), anti–β-tubulin (1:1,000 WB; ab6046; Abcam), anti-optineurin (1:1,000 WB, 1:200 IF; a gift from R. Weil, Institut Pasteur, Paris, France), anti-TYRP1 (1:1,000 WB; sc-25543; Santa Cruz), anti-WASH1 (1:500 WB, 1:200 IF; a gift from A. Gautreau, Ecole Polytechnique, Université Paris Saclay, Palaiseau, France), anti-strumpellin (1/1,000 WB; ab101222; Abcam), anti-Rab5 (1:1,000 WB; Cell Signaling Technology), anti-GFP (1:100 EM; A-11122; Invitrogen), anti-DNP (1:200 IF, 1:2,000 EM; Molecular Probes), anti-GAPDH (1:10,000 WB; G9545; Sigma); mouse anti-TYRP1 (1:200 IF, 1:40 EM; clone TA99; Abcam), anti-VAMP7 (1:1,000 WB; a gift from T. Galli, INSERM U894, Centre de Psychiatrie et Neurosciences, Paris, France), anti-cortactin (1:200 IF; clone 4F11; Millipore), anti-p34 (1:100 IF; a gift from P. Chavrier, Institut Curie, Paris, France), anti-HMB45 (1:200 IF; ab787; Abcam); sheep anti-EGFR (1:500 IF; 20-ES04; Fitzgerald); rat anti-GFP (1:1,000 WB; 3H9; Chromotek); HRP-conjugated goat anti–mouse, anti–rabbit, and anti–rat HRP (1:10,000 WB; ab6721, ab6789, and ab97057, respectively; Abcam), Alexa Fluor 488–, 555–, or 647–conjugated goat anti-rabbit and anti-mouse or donkey anti-goat, anti-rabbit, and anti-mouse (1:200 IF; Invitrogen); protein A conjugated to 10 or 15 nm gold particles (PAG; 1:50; Cell Microscopy Center, Utrecht University Hospital, Utrecht, Netherlands).

Plasmids

Plasmids encoding full-length wild-type GFP-Myo6 and GFP-Myo6-CBD (porcine isoform: UniProt F1RQI7) were obtained from E. Coudrier (Institut Curie, Paris, France; Loubéry et al., 2012); plasmids encoding mCh- and GFP-VAMP7 were from T. Galli; plasmids encoding GFP-TYRP1, TYRP1-RFP and GFP-Vps35 were from M.S. Marks (Children's Hospital of Philadelphia, Philadelphia, PA); and plasmids encoding GFP were from Clontech. A synthetic gene fragment designed to further decrease Myo6 siRNA targeting in the porcine context (#1: C**G**AC**T**CTGCT**G**CA-**C**AATAT; #2: **CT**TGAAAGA**C**CCT**T**TG**T**TA; #3: **T**AT**C**GT**T**TC**A**G-GT**G**A**G**TC**T**; #4: **C**AATCC**T**TA**T**TT**C**GA**T**ATA; bold indicates mismatch) was used to generate GFP-Myo6^{R} by Gibson assembly.

siRNAs

The sense strand for the indicated double-stranded siRNAs were synthesized with the following sequences (Qiagen): siCtrl, 5′-AAT TCTCCGAACGTGTCACGT-3′; siOptn, 5′-GGAGACTGTTGGAAG CGAAGT-3′. ON-TARGET plus SMARTpool siRNAs were used to target Myo6 and WASH1 (Dharmacon) as follows: siMyo6#1, 5′-CCACACUGCUCCAUAAUAU-3′; #2, 5′-UAUGAAAGAUCCUCU GCUA-3′; #3, 5′-CAUUGUAUCUGGAGAAUCA-3′; #4, 5′-GAAUCC AUACUUUGACAUA-3′; siWASH1#1, 5′-AGCAGGUCCCAGAGA ACUA-3′, #2, 5′-AGACCUAUGCCGUGCCCUU-3′; #3, 5′-GUGCAG GCCAUUGGAGAGA-3′; and #4, 5′-AGACCUACAAGAUGGGGUA-3′.

Reagents and drug treatment

Cells were incubated with TIP (Sigma-Aldrich) at 5 µM for 30 min for live cell imaging or for 60 min at 25 µM for EM. To stimulate

melanosome biogenesis and secretion, MNT-1 cells were incubated with 30 µM forskolin (Sigma-Aldrich) for 3 d. CK-666 and SMIFH2 (Tocris Biosciences) treatments were for 30 min at 50 µM. To inhibit myosin II activity, cells were incubated 60 min with 50 µM para-nitroblebbistatin (Optopharma; a gift from S. Miserey-Lenkei, Institut Curie, Paris, France). For the incubation with DAMP, cells were starved 30 min with serum-free medium (Opti-MEM; Thermo Fisher Scientific), incubated 30 min with 30 µM DAMP (Invitrogen) at 37°C, and then washed with cold medium before fixation.

Western blot

Cells were lysed on ice in lysis buffer (50 mM Tris, 150 mM NaCl, 0.1% Triton X-100, and 10 mM EDTA, pH 7.2) supplemented with a protease inhibitor cocktail (Roche). Lysates were incubated with sample buffer, boiled 5 min, loaded on 4–12% Bis-Tris gels (NuPAGE; Invitrogen), and transferred on nitrocellulose membranes (GE Healthcare). Membranes were blocked in PBS/0.1% Tween with 5% nonfat dried milk, incubated with indicated primary and secondary antibodies diluted in PBS/0.1% Tween. Western blots were developed using the ECL SuperSignal West Pico or Dura (Thermo Fisher Scientific). The presented immunoblots were representative of at least three independent experiments.

Immunoprecipitation

MNT-1 cells seeded on 10-cm dishes (two per condition) were transfected with respective GFP-fusion protein encoding plasmids. The day after, cells were lysed 20 min on ice in 1 ml IP buffer (25 mM Hepes, 50 mM NaCl, 1.5 mM $MgCl_2$, 2 mM $CaCl_2$, 5 mM EDTA, and 0.1% NP-40, pH 7.4, and supplemented with protease inhibitor cocktail; Roche). Cells were scrapped and the lysates were centrifuged 15 min at 13,200 rpm (4°C). 50 µl of the postnuclear supernatant was collected (input), whereas the rest was incubated for 2 h under rotation (4°C) with 10 µl prewashed GFP-Trap_A beads (Chromotek). Then, beads were washed three times in IP buffer, and inputs and beads were incubated with 50 µl and 40 µl of sample buffer, respectively, and boiled for 5 min. The presented immunoblots are representative of at least three independent experiments.

Melanosome isolation

MNT-1 cells seeded on 10-cm dishes (two per condition) were collected, pelleted, and suspended in melanosome buffer (25 mM Hepes, 1 mM EDTA, 0.1 M EGTA, and 0.02% sodium azide, pH 7.4) supplemented with 0.25 M sucrose and homogenized using a Dounce homogenizer. Lysates were centrifuged for 10 min at 600 *g* (4°C), and the supernatant was collected and loaded on 2 M sucrose diluted in melanosome buffer and centrifuged for 30 min at 11,000 *g* (4°C). The melanosome-enriched fraction was carefully recovered and centrifuged 60 min at 100,000 *g* (4°C). The pellet was suspended 20 min in lysis buffer on ice, the protein concentration was measured (Pierce BCA protein assay kit; Thermo Fisher Scientific), and samples were diluted to obtain similar concentration before Western blot analysis. The presented immunoblots are representative of at least three independent experiments.

Melanin estimation

For intracellular melanin content, MNT-1 cells seeded on 6-cm dishes were sonicated in melanin buffer (50 mM Tris, 2 mM EDTA, and 150 mM NaCl, pH 7.4) supplemented with protease inhibitor cocktail (Roche). Melanin was pelleted for 15 min at 16,000 *g* (4°C), rinsed in ethanol/diethyl ether (1:1), and dissolved in 2 M NaOH/20% DMSO at 60°C. The optical density at 490 nm was measured to estimate melanin content. For extracellular melanin, MNT-1 cells were seeded on 10-cm dishes at day 1, transfected with siRNAs on days 3 and 5, and incubated with 30 µM forskolin on day 5. Supernatants were recovered before each siRNA transfection and pooled on day 8 before centrifugation for 10 min at 600 *g* (4°C). Melanin was pelleted for 15 min at 16,000 *g* (4°C), washed carefully with ethanol/diethyl ether (1:1), and dissolved in 2 M NaOH/20% DMSO at 60°C. The optical density at 490 nm was measured and normalized to protein concentration. Intracellular melanin was quantified as well, and the secreted melanin corresponds to the ratio between extra- and intracellular melanin.

IF and superresolution microscopy

MNT-1 cells grown on coverslips were incubated for 30 s in PBS/0.02% Saponin to extract the cytosol and then fixed for 15 min at RT with 4% PFA. Cells were incubated with PBS/2% BSA (blocking buffer) and permeabilized in PBS/2% BSA/0.1% saponin (permeabilization buffer) before primary and secondary antibody incubation in permeabilization buffer. Cells were washed in permeabilizing buffer and then in blocking buffer, and coverslips were mounted in DABCO medium. Coverslips were analyzed on a wide-field microscope (Eclipse 80i Upright; Nikon) equipped with a CCD camera (CoolSNAP HQ2; Photometrics) using a 100× 1.4 NA Plan-Apo objective lens. Z images series were acquired every 0.2 µm with the piezoelectric motor (Physik Instrumente) using MetaMorph software (version 7.8.13; MDS Analytical Technologies). Raw images were deconvolved with Meinel algorithm (PICT-IBiSA imaging platform at Institut Curie). For transfer assay, coverslips were acquired on a wide-field microscope (Eclipse 90i Upright) equipped with a CCD camera (CoolSNAP HQ2) and using a 60× 1.4 NA Plan-Apo objective lens. Z images series were acquired every 0.2 µm with the piezoelectric motor (Physik Instrumente) using MetaMorph software (version 7.8.13). For superresolution microscopy, images were acquired on a spinning disk system (Gataca Systems) based on an inverted microscope (Ti-E; Nikon) equipped with a sCMOS camera (Prime 95B; Photometrics), a confocal spinning head (X1; Yokogawa), a 100× 1.4 NA Plan-Apo objective lens, and a superresolution module (Live-SR; Gataca systems) based on structured illumination with optical reassignment technique and online processing leading to a two-time resolution improvement (Roth and Heintzmann, 2016). The method, called multifocal structured illumination microscopy (York et al., 2012), allows combining the doubling resolution together with the physical optical sectioning of confocal microscopy. The maximum resolution is 128 nm with a pixel size in superresolution mode of 64 nm. For live-cell superresolution, cells were imaged in Opti-MEM medium at 37°C and 5% CO_2 using MetaMorph software (version 7.8.13).

Live-cell imaging

MNT-1 cells were seeded on a FluoroDish (World Precision Instruments) and imaged in Opti-MEM medium on an inverted microscope (Ti-E) with a confocal spinning head (X1) equipped with an EMCCD camera (iXon 897; Andor Technology), a 100× 1.4 NA Plan-Apo objective lens, and a temperature and CO_2 control system (37°C and 5% CO_2; Life Imaging Service). The acquisition parameters used were 200-ms exposure for GFP and mCherry channels. Movies were acquired on a single z plane for 40 s in stream mode, allowing acquisition at very fast rates, using MetaMorph software (version 7.8.13).

EM

MNT-1 cells cultured on carbonated sapphire disks or CryoCapsules (CryoCapCell; Heiligenstein et al., 2014) were transfected with control, Myo6, or WASH siRNAs or treated for 60 min with 25 µM DMSO or TIP. Cell were high-pressure frozen with HPM100 (Leica Microsystems) or HPM Live µ (CryoCapCell) and then freeze substituted in anhydrous acetone containing 1% OsO4/2% H_2O for 64 h in a freeze substitution system (AFS; Leica Microsystems). Cells were embedded in epon 812 (TAAB Laboratories Equipment) and processed for sectioning and contrasting with uranyl acetate and lead citrate. Ultrathin sections were observed at 80 kV transmission electron microscope (Tecnai Spirit G2; Thermo Fisher Scientific) equipped with a QUE MESA CCD camera (EMSIS) using iTEM software (EMSIS). For ultrathin cryosections and immunogold labeling, MNT-1 cells were grown on six-well plates and fixed with 2% PFA/0.2% glutaraldehyde/0.1 M phosphate buffer. Cells pellets were embedded in 10% gelatin and infused in 2.3 M sucrose. Gelatin blocks were frozen and processed for ultracryomicrotomy. Ultrathin sections (90 nm) were double-immunogold labeled using PAG 10 or 15 nm and analyzed by EM as described above.

CLEM

MNT-1 cells were grown on CryoCapsules (Heiligenstein et al., 2014) and transfected with GFP-Myo6-CBD. The day after, cells were high-pressure frozen using HPM100 (Leica Microsystems) and freeze-substituted for 12 h with 0.01% uranyl acetate/0.05% glutaraldehyde/1% H_2O in anhydrous acetone (Hurbain et al., 2017). Cells were embedded in Lowicryl and processed for sectioning. 300-nm-thick sections were mounted with Hoechst containing PBS/50% glycerol and analyzed with an epifluorescence microscope (Te2000; Nikon) equipped with a CoolSNAP HQ2 CCD camera using 60× 1.4 NA Plan-Apo objective lens. The fluorescent images were processed on ImageJ Fiji using the Smooth and Subtract Background commands, and the Extended Depth of Fields plugin. Sections were then acquired at the electron microscope, and fluorescent signal and electron micrograph were overlaid using eC-CLEM software (Paul-Gilloteaux et al., 2017) on Icy.

Electron tomography

Thick sections were randomly labeled on the two sides with PAG 10 nm. Tilt series (two perpendicular series, angular range from −60° to +65° with 1° increment) on area containing a GFP-Myo6-CBD$^+$ melanosome were recorded using EMtools (TVIPS) on a 200-kV transmission electron microscope (Tecnai 20 LaB6; Thermo Fisher Scientific) and used for reconstructing tomograms. Projection images (2,024 × 2,024 pixels) were acquired with CCD camera (Temcam F214; TVIPS). After acquisition of the first tilt series, the grid was rotated over an angle of 90° and the second tilt series of the same area was recorded. Tilt series alignment and tomogram computing (resolution-weighted back projection) were performed using eTomo (IMOD) software. PAG 10 nm at the surface of the sections was used as fiducial markers. Manual contouring of the melanosomal membrane of the tomograms was performed using IMOD.

Melanin transfer assay

NHMs seeded in 10-cm dishes at day 1 were transfected twice with control or Myo6 siRNAs at day 3 and day 5. At the end of day 5, NHMs were trypsinized, counted, and same amount were co-cultured with NHKs (1:1) on coverslips. NHKs alone were cultured on coverslips to estimate steady-state melanin content (see below). Because of the faster division rate of NHK as compared with NHMs, the NHM/NHK ratio is ∼1:5 at day 8. Cells were then fixed with 4% PFA and processed for IFM using anti-HMB45 (red; recognizing fibrils onto which melanin is deposited) and anti-EGFR (green; EGF receptor expressed only in NHKs) antibodies to label melanin and NHKs, respectively. Z-stacks images from bottom to top of NHK were acquired using wide-field microscope (see above). Maximum-intensity z projections of the stacks were generated for the two channels and background fluorescence intensity was subtracted from the total intensity. In the green channel, regions of interests were drawn to delineate NHKs, duplicated in the red channel to measure the mean intensity of fluorescence of HMB45 (ImageJ Fiji). Measurements were done in co-culture experiments and in single NHK culture. The mean intensity of HMB45 fluorescence obtained in single NHK culture was subtracted from the HMB45 fluorescence intensity measured in co-culture experiments. Percentage of HMB45$^+$ NHKs was defined as the number of NHKs with at least one HMB45 fluorescent spot divided by the total number of NHKs per experiment.

Image analysis and quantification

Analysis and quantification of mCh-VAMP7$^+$ tubules

mCh-VAMP7–expressing MNT-1 cells were analyzed on a spinning-disk microscope and acquired in stream mode for 40 s (200 frames at 200-ms exposure). Using ImageJ Fiji, 100 × 100–pixel (256-µm^2) regions were selected at cell periphery to detect isolated melanosomes. Images were processed using subtract background (50-pixel radius) and Smooth commands. The relative number of mCh-VAMP7$^+$ melanosomal tubules was manually counted during the 40-s acquisitions (corresponding to 200 frames of 0.2 s) in which they were observed. Among these tubules, the respective number of tubules that were detected as emerging (referred as tubules emerging from melanosomes) and/or detaching (referred as tubules undergoing fission) from melanosomes was quantified. The time of release corresponds to the mean number of frames per experiment during which the tubules were detected until their detachment from melanosomes and multiplied by 0.2 s (duration time of each frame) to obtain temporal values (s). The percentage of released tubules

was measured by dividing the number of tubules detaching from melanosomes by the total number of tubules detected per experiment.

Linescan analysis

MNT-1 cells coexpressing GFP-Myo6-CBD and mCh-VAMP7 were analyzed by live SR-FM. On mCh-VAMP7$^+$ melanosomes positive for GFP-Myo6-CBD and harboring a tubule, a line selection of 30 pixels (1,920 nm) was drawn across the melanosome and its associated tubule on ImageJ Fiji. Linear pixels values were measured using Plot Profile function and presented as percentage of the maximum value. For fixed cells analyzed by SR-IFM, a line selection of 30 pixels (1,920 nm) was drawn across a TYRP1$^+$ melanosome and one associated spot of the indicated protein.

Spot detection

Spots of endogenous Myo6, optineurin, WASH1, p34, or cortactin per melanosome were detected using Spot Detector plugin on Icy. 15-pixel (960-nm)-diameter circles were drawn around TYRP1$^+$ melanosomes and the number of detected spots per circle was measured. The percentage of melanosomes$^+$ for spots corresponds to the number of melanosomes with at least one spot divided by the total number of melanosomes analyzed per cell.

Pearson's correlation coefficient

Pearson's correlation coefficient between two channels was quantified using JACoP plugin of ImageJ Fiji from one frame of the live-cell acquisition. As a negative control, similar measures were performed after 30° rotation of the GFP channel on the same images.

GFP-Myo6-CBD spots associated with melanosome

MNT-1 cells transfected with GFP-Myo6-CBD and mCh-VAMP7 were analyzed by spinning-disk microscopy. Images were processed using the Subtract Background command (3- and 10-pixel radius for GFP and mCherry channels, respectively) on ImageJ Fiji. A random selection of GFP-Myo6-CBD$^+$ spots were analyzed per cell and considered as associated with melanosome if they displayed overlapping pixels with mCh-VAMP7. The number of GFP-Myo6-CBD spots that associated with melanosomes was then divided by the total number of spots analyzed per cell and was expressed as a percentage.

Overlapping spots at melanosome and Manders overlap coefficient

MNT-1 cells expressing GFP-Myo6-CBD were processed by SR-IFM using anti-TYRP1 (blue; to label melanosomes) and anti–optineurin or anti–WASH1 (red) antibodies. Z-stacks images were acquired every 0.15 µm. 15-pixel (960-nm)–diameter circles were drawn around melanosomes positive for Myo6/optineurin or Myo6/WASH1. Maximum intensity z projections of three stacks were generated for the three channels in the 15-pixel circles. Number of these melanosomes with overlapping pixels between green and red channels was measured, and this number was then divided by the total number of quantified melanosomes per cell and expressed as a percentage. On these melanosomes, the Manders overlap coefficient was quantified using JACoP plugin on ImageJ Fiji and corresponds to the fraction of the green signal (Myo6) overlapping with the red signal (optineurin or WASH1).

Quantification and analysis of tubules on EM sections

Quantification of tubules was based on their ultrastructure; a tubular membrane in continuity with the limiting membrane of melanosome was defined as a tubule connected to melanosome. Number of melanosomes with tubule per cell was quantified manually and divided by the total number of pigmented melanosomes per cell and was expressed as a percentage. The length of tubules was measured by drawing a line from the base to the extremity of the tubule, and the width of the neck by drawing a line covering the base (corresponding to the neck) of the tubule. To determine the orientation of the melanosomal tubule relative to the internal fibrils, two lines were drawn: one along the long axis of the internal fibrils within melanosome (and referred to 0°) and a second crossing the tubule along its maximum length. The angle between the two lines was measured using Icy. Tubules from control or Myo6-depleted cells were analyzed.

Immunogold labeling

Quantification of immunogold labeling on ultrathin cryosections was performed by counting the number of gold particles per pigmented melanosome. Pigmented melanosomes were defined by their morphology and the presence of electron dense melanin in their lumen (Raposo et al., 2001). Number of melanosomes stained with at least one gold particle was divided by the total number of melanosomes counted per cell and per section. The count was performed on randomly selected cells.

Immunoblot quantification

Quantification of protein expression levels on immunoblot was performed using ImageJ Fiji software and intensities were normalized to the siCtrl bands. Quantifications were from at least three independent experiments.

Statistical analysis

Statistical data are presented as mean ± SEM. Statistics were calculated using unpaired Student's *t* test, or ordinary one-way ANOVA when specified, in GraphPad Prism. Significant differences between control or treated samples are indicated (****, $P < 0.0001$; ***, $P < 0.001$; **, $P < 0.01$; *, $P < 0.05$). Only $P < 0.05$ was considered as statistically significant.

Online supplemental material

Fig. S1 shows the localization of mCh-VAMP7, GFP-Myo6, and GFP-Myo6-CBD to melanosomes in MNT-1 cells, associated quantifications and additional controls. Fig. S2 shows endogenous localization of Myo6 and optineurin to melanosomes in NHMs and MNT-1 cells and association of Myo6 to melanosomes in siOptn MNT-1 cells. Fig. S3 shows the ultrastructure of pigmented melanosomes and orientation of melanosomal tubules in MNT-1 cells treated or not with siMyo6 or TIP. Fig. S4 shows the localization of cortactin, p34, Myo6, and WASH1 in MNT-1 cells, the dynamics of mCh-VAMP7 in MNT-1 cells treated or not with CK-666 or SMIFH2 and the biochemical association between GFP-Myo6-CBD and strumpellin. Fig. S5 shows the characterization

of the pigmentation phenotype in optineurin-, Myo6-, and WASH1-depleted MNT-1 cells. Videos 1 and 2 show time-lapse imaging of mCh-VAMP7+ melanosomal tubule dynamics in non-treated (Video 1) or Myo6-depleted (Video 2) MNT-1 cells. Video 3 shows time-lapse imaging of the dynamics of GFP-Myo6 relative to mCh-VAMP7+ melanosomal tubule. Video 4 shows time-lapse imaging of mCh-VAMP7+ melanosomal tubule dynamics in TIP-treated MNT-1 cells. Video 5 shows the dynamics of mCh-VAMP7+ melanosomal tubule in GFP-Myo6-CBD expressing MNT-1 cells. Video 6 shows the 3D reconstructed model of a GFP-Myo6-CBD+ pigmented melanosomes identified using the CLEM-3D tomography procedure. Videos 7 and 8 show the dynamics of mCh-VAMP7+ melanosomal tubules in MNT-1 cells treated with CK-666 (Video 7) or depleted of WASH1 (Video 8).

Acknowledgments

We are grateful to Drs. Folma Buss, Thierry Galli, Evelyne Coudrier, Stéphanie Miserey-Lenkei, Philippe Chavrier, Alexis Gautreau, and Robert Weil for their gifts of reagents; Thibault Chastel for help with figure design using MATLAB; the Structure and Membrane Compartment laboratory for insightful discussions; and Lucie Sengmanivong, Vincent Fraisier, Ludovic Leconte (Centre National de la Recherche Scientifique, UMR 144, Institut Curie), and Charles Gueudry (Gataca Systems) for image acquisition, deconvolution, and superresolution. The authors greatly acknowledge the Nikon Imaging Center at Institut Curie/Centre National de la Recherche Scientifique and the PICT-IBiSA, a member of the France-BioImaging national research infrastructure (ANR10-INBS-04).

This work has received support under the program "Investissement d'Avenir" launched by the French Government and implemented by the Agence Nationale de la Recherche (ANR) with the references ANR-10-LBX-0038 and ANR-10-IDEX-0001-02 PSL, Fondation pour la Recherche Médicale (Equipe FRM DEQ20140329491 Team label to G. Raposo), the National Institutes of Health (2RO1IEY015625 to M.S. Marks and G. Raposo), ANR "MYOACTIONS" (ANR-17-CE11-0029-03 to C. Delevoye and A. Houdusse), the Fondation ARC pour la Recherche sur le Cancer (PJA20161204965 to C. Delevoye and DOC20160604404 to L. Ripoll), Labex CelTisPhyBio (to L. Ripoll, L. Domingues, and K.J. Petersen), Université Paris Diderot (to L. Ripoll), École Normale Supérieure de Lyon (to F. Fignon), Centre National de la Recherche Scientifique, Institut National de la Santé et de la Recherche Medicale, and Institut Curie.

The authors declare no competing financial interests.

Author contributions: L. Ripoll performed most of the experiments. X. Heiligenstein and I. Hurbain assisted in HPF, CLEM, and electron tomography. L. Domingues performed and analyzed the co-culture experiments. L. Ripoll and F. Figon performed and analyzed SR-IFM and IEM experiments. K.J. Petersen generated constructs; this work followed from prepublished results by M.K. Dennis and M.S. Marks. L. Ripoll and C. Delevoye designed and analyzed the experiments, assembled figures, and wrote the manuscript. All authors revised and edited the manuscript. C. Delevoye supervised the overall research and funded it together with A. Houdusse, M.S. Marks, and G. Raposo.

Submitted: 12 September 2017
Revised: 16 March 2018
Accepted: 9 May 2018

References

Aghamohammadzadeh, S., and K.R. Ayscough. 2009. Differential requirements for actin during yeast and mammalian endocytosis. *Nat. Cell Biol.* 11:1039–1042. https://doi.org/10.1038/ncb1918

Altman, D., H.L. Sweeney, and J.A. Spudich. 2004. The mechanism of myosin VI translocation and its load-induced anchoring. *Cell.* 116:737–749. https://doi.org/10.1016/S0092-8674(04)00211-9

Ambrosio, A.L., J.A. Boyle, A.E. Aradi, K.A. Christian, and S.M. Di Pietro. 2016. TPC2 controls pigmentation by regulating melanosome pH and size. *Proc. Natl. Acad. Sci. USA.* 113:5622–5627. https://doi.org/10.1073/pnas.1600108113

Anderson, R.G.W., J.R. Falck, J.L. Goldstein, and M.S. Brown. 1984. Visualization of acidic organelles in intact cells by electron microscopy. *Proc. Natl. Acad. Sci. USA.* 81:4838–4842. https://doi.org/10.1073/pnas.81.15.4838

Anitei, M., and B. Hoflack. 2011. Bridging membrane and cytoskeleton dynamics in the secretory and endocytic pathways. *Nat. Cell Biol.* 14:11–19. https://doi.org/10.1038/ncb2409

Aschenbrenner, L., T. Lee, and T. Hasson. 2003. Myo6 facilitates the translocation of endocytic vesicles from cell peripheries. *Mol. Biol. Cell.* 14:2728–2743. https://doi.org/10.1091/mbc.e02-11-0767

Au, J.S., C. Puri, G. Ihrke, J. Kendrick-Jones, and F. Buss. 2007. Myosin VI is required for sorting of AP-1B-dependent cargo to the basolateral domain in polarized MDCK cells. *J. Cell Biol.* 177:103–114. https://doi.org/10.1083/jcb.200608126

Bellono, N.W., I.E. Escobar, A.J. Lefkovith, M.S. Marks, and E. Oancea. 2014. An intracellular anion channel critical for pigmentation. *eLife.* 3:e04543. https://doi.org/10.7554/eLife.04543

Bellono, N.W., I.E. Escobar, and E. Oancea. 2016. A melanosomal two-pore sodium channel regulates pigmentation. *Sci. Rep.* 6:26570. https://doi.org/10.1038/srep26570

Bissig, C., L. Rochin, and G. van Niel. 2016. PMEL Amyloid Fibril Formation: The Bright Steps of Pigmentation. *Int. J. Mol. Sci.* 17:1438. https://doi.org/10.3390/ijms17091438

Bonazzi, M., L. Vasudevan, A. Mallet, M. Sachse, A. Sartori, M.C. Prevost, A. Roberts, S.B. Taner, J.D. Wilbur, F.M. Brodsky, and P. Cossart. 2011. Clathrin phosphorylation is required for actin recruitment at sites of bacterial adhesion and internalization. *J. Cell Biol.* 195:525–536. https://doi.org/10.1083/jcb.201105152

Bond, L.M., A.A. Peden, J. Kendrick-Jones, J.R. Sellers, and F. Buss. 2011. Myosin VI and its binding partner optineurin are involved in secretory vesicle fusion at the plasma membrane. *Mol. Biol. Cell.* 22:54–65. https://doi.org/10.1091/mbc.e10-06-0553

Boulant, S., C. Kural, J.C. Zeeh, F. Ubelmann, and T. Kirchhausen. 2011. Actin dynamics counteract membrane tension during clathrin-mediated endocytosis. *Nat. Cell Biol.* 13:1124–1131. https://doi.org/10.1038/ncb2307

Brenner, M., and V.J. Hearing. 2008. Modifying skin pigmentation - approaches through intrinsic biochemistry and exogenous agents. *Drug Discov. Today Dis. Mech.* 5:e189–e199. https://doi.org/10.1016/j.ddmec.2008.02.001

Brooks, A.B., D. Humphreys, V. Singh, A.C. Davidson, S.D. Arden, F. Buss, and V. Koronakis. 2017. MYO6 is targeted by *Salmonella* virulence effectors to trigger PI3-kinase signaling and pathogen invasion into host cells. *Proc. Natl. Acad. Sci. USA.* 114:3915–3920. https://doi.org/10.1073/pnas.1616418114

Buckley, C.M., N. Gopaldass, C. Bosmani, S.A. Johnston, T. Soldati, R.H. Insall, and J.S. King. 2016. WASH drives early recycling from macropinosomes and phagosomes to maintain surface phagocytic receptors. *Proc. Natl. Acad. Sci. USA.* 113:E5906–E5915. https://doi.org/10.1073/pnas.1524532113

Bultema, J.J., J.A. Boyle, P.B. Malenke, F.E. Martin, E.C. Dell'Angelica, R.E. Cheney, and S.M. Di Pietro. 2014. Myosin vc interacts with Rab32 and Rab38 proteins and works in the biogenesis and secretion of melanosomes. *J. Biol. Chem.* 289:33513–33528. https://doi.org/10.1074/jbc.M114.578948

Buss, F., S.D. Arden, M. Lindsay, J.P. Luzio, and J. Kendrick-Jones. 2001. Myosin VI isoform localized to clathrin-coated vesicles with a role in clathrin-mediated endocytosis. *EMBO J.* 20:3676–3684. https://doi.org/10.1093/emboj/20.14.3676

Carnell, M., T. Zech, S.D. Calaminus, S. Ura, M. Hagedorn, S.A. Johnston, R.C. May, T. Soldati, L.M. Machesky, and R.H. Insall. 2011. Actin polymerization driven by WASH causes V-ATPase retrieval and vesicle neutralization before exocytosis. *J. Cell Biol.* 193:831–839. https://doi.org/10.1083/jcb.201009119

Cheng, J., A. Grassart, and D.G. Drubin. 2012. Myosin 1E coordinates actin assembly and cargo trafficking during clathrin-mediated endocytosis. *Mol. Biol. Cell.* 23:2891–2904. https://doi.org/10.1091/mbc.e11-04-0383

Chibalina, M.V., M.N. Seaman, C.C. Miller, J. Kendrick-Jones, and F. Buss. 2007. Myosin VI and its interacting protein LMTK2 regulate tubule formation and transport to the endocytic recycling compartment. *J. Cell Sci.* 120:4278–4288. https://doi.org/10.1242/jcs.014217

Cureton, D.K., R.H. Massol, S. Saffarian, T.L. Kirchhausen, and S.P. Whelan. 2009. Vesicular stomatitis virus enters cells through vesicles incompletely coated with clathrin that depend upon actin for internalization. *PLoS Pathog.* 5:e1000394. https://doi.org/10.1371/journal.ppat.1000394

Dance, A.L., M. Miller, S. Seragaki, P. Aryal, B. White, L. Aschenbrenner, and T. Hasson. 2004. Regulation of myosin-VI targeting to endocytic compartments. *Traffic.* 5:798–813. https://doi.org/10.1111/j.1600-0854.2004.00224.x

Delevoye, C. 2014. Melanin transfer: the keratinocytes are more than gluttons. *J. Invest. Dermatol.* 134:877–879. https://doi.org/10.1038/jid.2013.487

Delevoye, C., X. Heiligenstein, L. Ripoll, F. Gilles-Marsens, M.K. Dennis, R.A. Linares, L. Derman, A. Gokhale, E. Morel, V. Faundez, et al. 2016. BLOC-1 Brings Together the Actin and Microtubule Cytoskeletons to Generate Recycling Endosomes. *Curr. Biol.* 26:1–13. https://doi.org/10.1016/j.cub.2015.11.020

Dennis, M.K., C. Delevoye, A. Acosta-Ruiz, I. Hurbain, M. Romao, G.G. Hesketh, P.S. Goff, E.V. Sviderskaya, D.C. Bennett, J.P. Luzio, et al. 2016. BLOC-1 and BLOC-3 regulate VAMP7 cycling to and from melanosomes via distinct tubular transport carriers. *J. Cell Biol.* 214:293–308. https://doi.org/10.1083/jcb.201605090

Derivery, E., C. Sousa, J.J. Gautier, B. Lombard, D. Loew, and A. Gautreau. 2009. The Arp2/3 activator WASH controls the fission of endosomes through a large multiprotein complex. *Dev. Cell.* 17:712–723. https://doi.org/10.1016/j.devcel.2009.09.010

Derivery, E., E. Helfer, V. Henriot, and A. Gautreau. 2012. Actin polymerization controls the organization of WASH domains at the surface of endosomes. *PLoS One.* 7:e39774. https://doi.org/10.1371/journal.pone.0039774

De Vos, K.J., V.J. Allan, A.J. Grierson, and M.P. Sheetz. 2005. Mitochondrial function and actin regulate dynamin-related protein 1-dependent mitochondrial fission. *Curr. Biol.* 15:678–683. https://doi.org/10.1016/j.cub.2005.02.064

Duleh, S.N., and M.D. Welch. 2012. Regulation of integrin trafficking, cell adhesion, and cell migration by WASH and the Arp2/3 complex. *Cytoskeleton (Hoboken).* 69:1047–1058. https://doi.org/10.1002/cm.21069

Ferguson, S.M., A. Raimondi, S. Paradise, H. Shen, K. Mesaki, A. Ferguson, O. Destaing, G. Ko, J. Takasaki, O. Cremona, et al. 2009. Coordinated actions of actin and BAR proteins upstream of dynamin at endocytic clathrin-coated pits. *Dev. Cell.* 17:811–822. https://doi.org/10.1016/j.devcel.2009.11.005

Gasman, S., S. Chasserot-Golaz, M. Malacombe, M. Way, and M.F. Bader. 2004. Regulated exocytosis in neuroendocrine cells: a role for subplasmalemmal Cdc42/N-WASP-induced actin filaments. *Mol. Biol. Cell.* 15:520–531. https://doi.org/10.1091/mbc.e03-06-0402

Gautreau, A., K. Oguievetskaia, and C. Ungermann. 2014. Function and regulation of the endosomal fusion and fission machineries. *Cold Spring Harb. Perspect. Biol.* 6:6. https://doi.org/10.1101/cshperspect.a016832

Gerondopoulos, A., L. Langemeyer, J.R. Liang, A. Linford, and F.A. Barr. 2012. BLOC-3 mutated in Hermansky-Pudlak syndrome is a Rab32/38 guanine nucleotide exchange factor. *Curr. Biol.* 22:2135–2139. https://doi.org/10.1016/j.cub.2012.09.020

Gomez, T.S., and D.D. Billadeau. 2009. A FAM21-containing WASH complex regulates retromer-dependent sorting. *Dev. Cell.* 17:699–711. https://doi.org/10.1016/j.devcel.2009.09.009

Gomez, T.S., J.A. Gorman, A.A. de Narvajas, A.O. Koenig, and D.D. Billadeau. 2012. Trafficking defects in WASH-knockout fibroblasts originate from collapsed endosomal and lysosomal networks. *Mol. Biol. Cell.* 23:3215–3228. https://doi.org/10.1091/mbc.e12-02-0101

Harbour, M.E., S.Y. Breusegem, and M.N. Seaman. 2012. Recruitment of the endosomal WASH complex is mediated by the extended 'tail' of Fam21 binding to the retromer protein Vps35. *Biochem. J.* 442:209–220. https://doi.org/10.1042/BJ20111761

Heiligenstein, X., J. Heiligenstein, C. Delevoye, I. Hurbain, S. Bardin, P. Paul-Gilloteaux, L. Sengmanivong, G. Régnier, J. Salamero, C. Antony, and G. Raposo. 2014. The CryoCapsule: simplifying correlative light to electron microscopy. *Traffic.* 15:700–716. https://doi.org/10.1111/tra.12164

Heissler, S.M., J. Selvadurai, L.M. Bond, R. Fedorov, J. Kendrick-Jones, F. Buss, and D.J. Manstein. 2012. Kinetic properties and small-molecule inhibition of human myosin-6. *FEBS Lett.* 586:3208–3214. https://doi.org/10.1016/j.febslet.2012.07.014

Hetrick, B., M.S. Han, L.A. Helgeson, and B.J. Nolen. 2013. Small molecules CK-666 and CK-869 inhibit actin-related protein 2/3 complex by blocking an activating conformational change. *Chem. Biol.* 20:701–712. https://doi.org/10.1016/j.chembiol.2013.03.019

Hurbain, I., W.J. Geerts, T. Boudier, S. Marco, A.J. Verkleij, M.S. Marks, and G. Raposo. 2008. Electron tomography of early melanosomes: implications for melanogenesis and the generation of fibrillar amyloid sheets. *Proc. Natl. Acad. Sci. USA.* 105:19726–19731. https://doi.org/10.1073/pnas.0803488105

Hurbain, I., M. Romao, P. Bergam, X. Heiligenstein, and G. Raposo. 2017. Analyzing lysosome-related organelles by electron microscopy. *Methods Mol. Biol.* 1594:43–71. https://doi.org/10.1007/978-1-4939-6934-0_4

Idrissi, F.Z., A. Blasco, A. Espinal, and M.I. Geli. 2012. Ultrastructural dynamics of proteins involved in endocytic budding. *Proc. Natl. Acad. Sci. USA.* 109:E2587–E2594. https://doi.org/10.1073/pnas.1202789109

Jani, R.A., L.K. Purushothaman, S. Rani, P. Bergam, and S.R. Setty. 2015. STX13 regulates cargo delivery from recycling endosomes during melanosome biogenesis. *J. Cell Sci.* 128:3263–3276. https://doi.org/10.1242/jcs.171165

Jonsdottir, G.A., and R. Li. 2004. Dynamics of yeast Myosin I: evidence for a possible role in scission of endocytic vesicles. *Curr. Biol.* 14:1604–1609. https://doi.org/10.1016/j.cub.2004.08.055

King, J.S., A. Gueho, M. Hagedorn, N. Gopaldass, F. Leuba, T. Soldati, and R.H. Insall. 2013. WASH is required for lysosomal recycling and efficient autophagic and phagocytic digestion. *Mol. Biol. Cell.* 24:2714–2726. https://doi.org/10.1091/mbc.e13-02-0092

Krendel, M., E.K. Osterweil, and M.S. Mooseker. 2007. Myosin 1E interacts with synaptojanin-1 and dynamin and is involved in endocytosis. *FEBS Lett.* 581:644–650. https://doi.org/10.1016/j.febslet.2007.01.021

Kukulski, W., M. Schorb, S. Welsch, A. Picco, M. Kaksonen, and J.A. Briggs. 2011. Correlated fluorescence and 3D electron microscopy with high sensitivity and spatial precision. *J. Cell Biol.* 192:111–119. https://doi.org/10.1083/jcb.201009037

Limouze, J., A.F. Straight, T. Mitchison, and J.R. Sellers. 2004. Specificity of blebbistatin, an inhibitor of myosin II. *J. Muscle Res. Cell Motil.* 25:337–341. https://doi.org/10.1007/s10974-004-6060-7

Liu, J., M. Kaksonen, D.G. Drubin, and G. Oster. 2006. Endocytic vesicle scission by lipid phase boundary forces. *Proc. Natl. Acad. Sci. USA.* 103:10277–10282. https://doi.org/10.1073/pnas.0601045103

Liu, Y., X.H. Xu, Q. Chen, T. Wang, C.Y. Deng, B.L. Song, J.L. Du, and Z.G. Luo. 2013. Myosin Vb controls biogenesis of post-Golgi Rab10 carriers during axon development. *Nat. Commun.* 4:2005. https://doi.org/10.1038/ncomms3005

Lo Cicero, A., C. Delevoye, F. Gilles-Marsens, D. Loew, F. Dingli, C. Guéré, N. André, K. Vié, G. van Niel, and G. Raposo. 2015. Exosomes released by keratinocytes modulate melanocyte pigmentation. *Nat. Commun.* 6:7506. https://doi.org/10.1038/ncomms8506

Loubéry, S., C. Delevoye, D. Louvard, G. Raposo, and E. Coudrier. 2012. Myosin VI regulates actin dynamics and melanosome biogenesis. *Traffic.* 13:665–680. https://doi.org/10.1111/j.1600-0854.2012.01342.x

Marks, M.S., H.F. Heijnen, and G. Raposo. 2013. Lysosome-related organelles: unusual compartments become mainstream. *Curr. Opin. Cell Biol.* 25:495–505. https://doi.org/10.1016/j.ceb.2013.04.008

Miserey-Lenkei, S., G. Chalancon, S. Bardin, E. Formstecher, B. Goud, and A. Echard. 2010. Rab and actomyosin-dependent fission of transport vesicles at the Golgi complex. *Nat. Cell Biol.* 12:645–654. https://doi.org/10.1038/ncb2067

Murk, J.L., G. Posthuma, A.J. Koster, H.J. Geuze, A.J. Verkleij, M.J. Kleijmeer, and B.M. Humbel. 2003. Influence of aldehyde fixation on the morphology of endosomes and lysosomes: quantitative analysis and electron tomography. *J. Microsc.* 212:81–90. https://doi.org/10.1046/j.1365-2818.2003.01238.x

Naccache, S.N., T. Hasson, and A. Horowitz. 2006. Binding of internalized receptors to the PDZ domain of GIPC/synectin recruits myosin VI to endocytic vesicles. *Proc. Natl. Acad. Sci. USA.* 103:12735–12740. https://doi.org/10.1073/pnas.0605317103

Nolen, B.J., N. Tomasevic, A. Russell, D.W. Pierce, Z. Jia, C.D. McCormick, J. Hartman, R. Sakowicz, and T.D. Pollard. 2009. Characterization of two classes of small molecule inhibitors of Arp2/3 complex. *Nature.* 460:1031–1034. https://doi.org/10.1038/nature08231

Patwardhan, A., and C. Delevoye. 2016. Ions switch off darkness: role of TPC2 in melanosomes. *Pigment Cell Melanoma Res.* 29:498–499. https://doi.org/10.1111/pcmr.12510

Patwardhan, A., S. Bardin, S. Miserey-Lenkei, L. Larue, B. Goud, G. Raposo, and C. Delevoye. 2017. Routing of the RAB6 secretory pathway towards the lysosome related organelle of melanocytes. *Nat. Commun.* 8:15835. https://doi.org/10.1038/ncomms15835

Paul-Gilloteaux, P., X. Heiligenstein, M. Belle, M.C. Domart, B. Larijani, L. Collinson, G. Raposo, and J. Salamero. 2017. eC-CLEM: flexible multidimensional registration software for correlative microscopies. *Nat. Methods.* 14:102–103. https://doi.org/10.1038/nmeth.4170

Raposo, G., D. Tenza, D.M. Murphy, J.F. Berson, and M.S. Marks. 2001. Distinct protein sorting and localization to premelanosomes, melanosomes, and lysosomes in pigmented melanocytic cells. *J. Cell Biol.* 152:809–824. https://doi.org/10.1083/jcb.152.4.809

Ripoll, L., X. Heiligenstein, G. Raposo, and C. Delevoye. 2016. Illuminating the dark side of recycling endosomes. *Cell Cycle.* 15:1309–1310. https://doi.org/10.1080/15384101.2016.1160682

Rizvi, S.A., E.M. Neidt, J. Cui, Z. Feiger, C.T. Skau, M.L. Gardel, S.A. Kozmin, and D.R. Kovar. 2009. Identification and characterization of a small molecule inhibitor of formin-mediated actin assembly. *Chem. Biol.* 16:1158–1168. https://doi.org/10.1016/j.chembiol.2009.10.006

Römer, W., L.L. Pontani, B. Sorre, C. Rentero, L. Berland, V. Chambon, C. Lamaze, P. Bassereau, C. Sykes, K. Gaus, and L. Johannes. 2010. Actin dynamics drive membrane reorganization and scission in clathrin-independent endocytosis. *Cell.* 140:540–553. https://doi.org/10.1016/j.cell.2010.01.010

Roth, S., and R. Heintzmann. 2016. Optical photon reassignment with increased axial resolution by structured illumination. *Methods Appl. Fluoresc.* 4:045005. https://doi.org/10.1088/2050-6120/4/4/045005

Sahlender, D.A., R.C. Roberts, S.D. Arden, G. Spudich, M.J. Taylor, J.P. Luzio, J. Kendrick-Jones, and F. Buss. 2005. Optineurin links myosin VI to the Golgi complex and is involved in Golgi organization and exocytosis. *J. Cell Biol.* 169:285–295. https://doi.org/10.1083/jcb.200501162

Schnoor, M., T.E. Stradal, and K. Rottner. 2018. Cortactin: Cell Functions of A Multifaceted Actin-Binding Protein. *Trends Cell Biol.* 28:79–98. https://doi.org/10.1016/j.tcb.2017.10.009

Seaman, M.N., A. Gautreau, and D.D. Billadeau. 2013. Retromer-mediated endosomal protein sorting: all WASHed up! *Trends Cell Biol.* 23:522–528. https://doi.org/10.1016/j.tcb.2013.04.010

Simunovic, M., J.B. Manneville, H.F. Renard, E. Evergren, K. Raghunathan, D. Bhatia, A.K. Kenworthy, G.A. Voth, J. Prost, H.T. McMahon, et al. 2017. Friction Mediates Scission of Tubular Membranes Scaffolded by BAR Proteins. *Cell.* 170:172–184.

Singh, S.K., C. Nizard, R. Kurfurst, F. Bonte, S. Schnebert, and D.J. Tobin. 2008. The silver locus product (Silv/gp100/Pmel17) as a new tool for the analysis of melanosome transfer in human melanocyte-keratinocyte co-culture. *Exp. Dermatol.* 17:418–426. https://doi.org/10.1111/j.1600-0625.2008.00702.x

Sirotkin, V., C.C. Beltzner, J.B. Marchand, and T.D. Pollard. 2005. Interactions of WASp, myosin-I, and verprolin with Arp2/3 complex during actin patch assembly in fission yeast. *J. Cell Biol.* 170:637–648. https://doi.org/10.1083/jcb.200502053

Slowicka, K., L. Vereecke, and G. van Loo. 2016. Cellular Functions of Optineurin in Health and Disease. *Trends Immunol.* 37:621–633. https://doi.org/10.1016/j.it.2016.07.002

Spudich, G., M.V. Chibalina, J.S. Au, S.D. Arden, F. Buss, and J. Kendrick-Jones. 2007. Myosin VI targeting to clathrin-coated structures and dimerization is mediated by binding to Disabled-2 and PtdIns(4,5)P2. *Nat. Cell Biol.* 9:176–183. https://doi.org/10.1038/ncb1531

Straight, A.F., A. Cheung, J. Limouze, I. Chen, N.J. Westwood, J.R. Sellers, and T.J. Mitchison. 2003. Dissecting temporal and spatial control of cytokinesis with a myosin II Inhibitor. *Science.* 299:1743–1747. https://doi.org/10.1126/science.1081412

Sundaramoorthy, V., A.K. Walker, V. Tan, J.A. Fifita, E.P. Mccann, K.L. Williams, I.P. Blair, G.J. Guillemin, M.A. Farg, and J.D. Atkin. 2015. Defects in optineurin- and myosin VI-mediated cellular trafficking in amyotrophic lateral sclerosis. *Hum. Mol. Genet.* 24:3830–3846. https://doi.org/10.1093/hmg/ddv126

Tabata, H., N. Kawamura, G.H. Sun-Wada, and Y. Wada. 2008. Vacuolar-type H(+)-ATPase with the a3 isoform is the proton pump on premature melanosomes. *Cell Tissue Res.* 332:447–460. https://doi.org/10.1007/s00441-008-0597-5

Taylor, M.J., M. Lampe, and C.J. Merrifield. 2012. A feedback loop between dynamin and actin recruitment during clathrin-mediated endocytosis. *PLoS Biol.* 10:e1001302. https://doi.org/10.1371/journal.pbio.1001302

Thomason, P.A., J.S. King, and R.H. Insall. 2017. Mroh1, a lysosomal regulator localized by WASH-generated actin. *J. Cell Sci.* 130:1785–1795. https://doi.org/10.1242/jcs.197210

Tran, D.T., A. Masedunskas, R. Weigert, and K.G. Ten Hagen. 2015. Arp2/3-mediated F-actin formation controls regulated exocytosis in vivo. *Nat. Commun.* 6:10098. https://doi.org/10.1038/ncomms10098

Tumbarello, D.A., B.J. Waxse, S.D. Arden, N.A. Bright, J. Kendrick-Jones, and F. Buss. 2012. Autophagy receptors link myosin VI to autophagosomes to mediate Tom1-dependent autophagosome maturation and fusion with the lysosome. *Nat. Cell Biol.* 14:1024–1035. https://doi.org/10.1038/ncb2589

Tumbarello, D.A., J. Kendrick-Jones, and F. Buss. 2013. Myosin VI and its cargo adaptors - linking endocytosis and autophagy. *J. Cell Sci.* 126:2561–2570. https://doi.org/10.1242/jcs.095554

Tyrrell, B.J., E.F. Woodham, H.J. Spence, D. Strathdee, R.H. Insall, and L.M. Machesky. 2016. Loss of strumpellin in the melanocytic lineage impairs the WASH Complex but does not affect coat colour. *Pigment Cell Melanoma Res.* 29:559–571. https://doi.org/10.1111/pcmr.12506

Warner, C.L., A. Stewart, J.P. Luzio, K.P. Steel, R.T. Libby, J. Kendrick-Jones, and F. Buss. 2003. Loss of myosin VI reduces secretion and the size of the Golgi in fibroblasts from Snell's waltzer mice. *EMBO J.* 22:569–579. https://doi.org/10.1093/emboj/cdg055

Wells, A.L., A.W. Lin, L.Q. Chen, D. Safer, S.M. Cain, T. Hasson, B.O. Carragher, R.A. Milligan, and H.L. Sweeney. 1999. Myosin VI is an actin-based motor that moves backwards. *Nature.* 401:505–508. https://doi.org/10.1038/46835

Wu, X., and J.A. Hammer. 2014. Melanosome transfer: it is best to give and receive. *Curr. Opin. Cell Biol.* 29:1–7. https://doi.org/10.1016/j.ceb.2014.02.003

York, A.G., S.H. Parekh, D. Dalle Nogare, R.S. Fischer, K. Temprine, M. Mione, A.B. Chitnis, C.A. Combs, and H. Shroff. 2012. Resolution doubling in live, multicellular organisms via multifocal structured illumination microscopy. *Nat. Methods.* 9:749–754. https://doi.org/10.1038/nmeth.2025